Running title: A cargo-regulated transition point in endocytosis

Cargo licenses maturation of stalled endocytic sites through a regulatory checkpoint

Ross TA Pedersen[†], Julian E Hassinger[†], Paul Marchando, David G Drubin*

Department of Molecular and Cell Biology, University of California, Berkeley, Berkeley, CA 94720

[†]These authors contributed equally to this work
*Correspondence: drubin@berkeley.edu

Abstract

During Clathrin-mediated endocytosis (CME), over 50 different proteins assemble on the plasma membrane to reshape it into a cargo-laden vesicle. Studies of *Saccharomyces cerevisiae* traced a detailed timeline of assembly of the CME machinery. Assembly of this machinery is coordinated with cargo capture; however, which CME steps are regulated, and which steps are deterministic, is unknown. In this study, we quantitatively and spatially describe progression through the CME pathway. We pinpointed a regulatory transition point that governs progression from the initiation phase of CME to the internalization phase. Proximity to endocytic cargo appears to influence maturation through this transition point, and direct evidence supports the conclusion that progress is regulated by cargo. While previous studies in yeast and mammalian cells suggested that cargo regulates rates of CME initiation or frequency of abortive events, our data instead identify maturation through a specific step in the CME pathway as the regulatory site.

Introduction

Membrane trafficking processes require coordinated cargo capture and membrane reshaping. One such process is clathrin-mediated endocytosis (CME), which is the major trafficking route into the cell (Bitsikas et al., 2014). During this process, more than 50 proteins including clathrin and actin assemble on the cytoplasmic leaflet of the plasma membrane. These proteins deform the membrane into a deep pit that undergoes scission to become a cargo-laden cytoplasmic vesicle (Kaksonen and Roux, 2018). Numerous studies have suggested that cargo influences the rate of CME by modulating the proportion of endocytic sites that continue to completion as opposed to aborting precociously (Ehrlich et al., 2004; Liu et al., 2010; Loerke et al., 2009; Mettlen et al., 2010). However, this proposed mode of coordinating cargo capture with endocytic internalization has recently been called into question when studies of genome-edited mammalian cells failed to reveal widespread abortive CME events (Doyon et al., 2011; Hong et al., 2015). Thus, despite extensive knowledge of the proteins involved in this process and their order of assembly, how CME is regulated and which steps are subject to regulation remain unresolved. We set out to determine how individual events during CME are modulated to control transit through the pathway as a whole.

The budding yeast *S. cerevisiae* is an ideal organism for systematic studies of the CME pathway. Aside from practical advantages such as simplicity, highly tractable genetics, and accessible genome editing, budding yeast has a remarkably regular CME pathway that invariably proceeds to completion (Kaksonen et al., 2005, 2003). Over 50 proteins are recruited to every CME site in budding yeast with a nearly invariant order and with fairly regular kinetics (Lu et al., 2016).

Budding yeast CME proteins have been conceptually organized into several functional modules based on shared timing of recruitment, common functions, detailed dynamic behavior, and organization at CME sites (Figure 1A, Carroll et al., 2012; Kaksonen et al., 2005; Lu et al., 2016). Initially, proteins of the early and early coat modules bind to the inner leaflet of the plasma membrane, marking the presumptive CME site (Godlee and Kaksonen, 2013; Lu and Drubin, 2017; Stimpson et al., 2009). These proteins are followed by the intermediate coat proteins: the Hip1R homologue Sla2 and the epsins Ent1 and Ent2 (Carroll et al., 2012). The intermediate coat proteins bind to actin filaments and couple actin filament elongation to membrane invagination (Skruzny et al., 2012). Following the intermediate coat, late coat proteins, including the intersectin functional homologue Pan1/End3/Sla1 complex, recruit the endocytic actin assembly machinery consisting of proteins of the WASP/Myosin complex (Bradford et al., 2015; Sun et al., 2015). The WASP myosin complex in turn orchestrates a critical burst of actin assembly and myosin activity to bend the plasma membrane into a deep pit (Lewellyn et al., 2015; Manenschijn et al., 2019; Pedersen and Drubin, 2019; Sun et al., 2006). While the early, intermediate, and late coat proteins internalize with the plasma membrane, the early module proteins dissociate from CME sites around the time of actin assembly (Carroll et al., 2012). Filamentous actin recruits a host of actin binding proteins and disassembly factors, collectively referred to as the actin module. Around the same time, proteins of the scission module bind to the neck of the endocytic invagination, releasing the nascent vesicle. The timing (timescale of minutes) and modular organization of this process are conserved from yeast to mammals (Taylor et al., 2011).

Despite this detailed knowledge of the CME machinery, how key transitions in the process are triggered remains poorly understood (Figure 1A). The mechanism of endocytic site initiation is controversial and obscure (Brach et al., 2014; Cocucci et al., 2012; Godlee and Kaksonen, 2013; Henne et al., 2010). After initiation, the budding yeast early and early coat proteins persist on the plasma membrane for a variable period of time before recruitment of the late arriving coat components, which are reported to have more regular lifetimes (Carroll et al., 2012; Newpher et al., 2005; Peng et al., 2015a; Stimpson et al., 2009). Regulation of the transition from the variable early phase to the more regular late phase of the process is poorly understood. Finally, how the initiation of actin assembly at endocytic sites is put into motion is uncertain, although multiple mechanisms have been proposed (Daste et al., 2017; Johansen et al., 2016; Sun et al., 2017). We set out to shed new light on mechanisms governing progression through the CME pathway.

Here, we performed systematic live-cell imaging analyses of proteins in the budding yeast CME pathway. Our data quantitatively separate the CME pathway into an early phase and a late phase. The behavior of proteins in each phase predicts the behavior of others in the same phase, but not the behavior of proteins in the other phase. Further experiments lead us to propose that the presence of cargo accelerates the transition from the early phase to the late phase, so this regulatory transition is likely a cargo checkpoint. We propose that endocytic sites are initiated widely but mature to the late, internalization phase more readily in the presence of cargo.

Results

Systematic live-cell imaging of clathrin-mediated endocytosis reveals inherent variability in timing and abundance of protein recruitment

We took a systematic imaging approach to quantitatively describe progression though the CME pathway. While each of the proteins of the CME pathway imaged here had been imaged previously to determine a recruitment order, our aim was to perform a deeper quantitative analysis in the hopes of uncovering previously undetected features and relationships among the proteins. Recruitment order and timing in the budding yeast CME pathway were previously determined by many pair-wise imaging iterations using two-color fluorescence microscopy. Here we imaged CME protein recruitment timing relative to three reference proteins, providing an orthogonal approach to determining the recruitment order and relative timing.

We acquired live-cell two-color total internal reflection fluorescence microscopy (TIRFM) movies of budding yeast strains expressing nearly two dozen different fluorescent fusion proteins (Supplementary Table 1). Each yeast strain encoded an endocytic query protein tagged with GFP and a reference protein for various stages of progression through CME tagged with a red fluorophore. All proteins were endogenously tagged and expressed from their own promoters in the genome to avoid overexpression artifacts. We chose the Eps15 homologue Ede1, a key component of the early endocytic module (Carroll et al., 2012; Lu and Drubin, 2017; Stimpson et al., 2009), as a reference protein to report on CME site initiation. Sla1, a late-arriving endocytic coat protein (Kaksonen et al., 2003), was used as a reference protein to report on the transition from the variable stage of CME to the regular stage. Finally, we chose the actin binding protein Abp1, a reporter of endocytic actin networks in budding yeast (Kaksonen et al., 2003), to report on initiation of actin

assembly. All of these reference proteins are relatively abundant at endocytic sites (and hence bright). We chose TIRFM in lieu of the more standard imaging modality of widefield microscopy in a medial focal plane of yeast cells (Kaksonen et al., 2005, 2003). TIRFM has superior signal-to-noise as well as minimal photobleaching, although this comes at the cost of losing the ability to track the endocytic proteins once they move away from the plasma membrane during internalization. The benefits of TIRFM were especially important for faithfully detecting and tracking the early endocytic proteins, because they produce a dim, long-lived signal at CME sites. By imaging different GFP-tagged "query" proteins in two-color movies with common reference markers, we were able to compare the dynamics of a large subset of the presently known CME proteins at endocytic sites.

To chronicle progression through the CME pathway, we chose GFP-tagged query proteins from each endocytic module. We imaged the early module proteins Syp1 (an FCho homologue) and Hrr25 (a casein kinase homologue) and the early coat proteins Pal1 and Apl1 (a component of the AP-2 complex) with reference to the early protein Ede1 to capture the earliest stages of CME. We also imaged the early module proteins Ede1, Syp1, and Hrr25 and the early coat proteins Pal1 and Apl1 with reference to the late coat protein Sla1 to monitor the transition from the early stage of CME to the late stage. Finally, we imaged a large sample of CME proteins with reference to Abp1 to monitor the late stage of CME and the initiation of actin assembly in particular. We used Ede1 and Syp1 as representative early proteins; Sla2 (Hip1R) as a representative intermediate coat protein; Pan1 (intersectin) and Sla1 as representative late coat proteins; Las17 (Wiscott-aldrich syndrome protein, WASP), Bzz1 (toca1), Vrp1 (WASP interacting protein, WIP), and Myo5 (myosin 1e) as representative WASP/Myosin module proteins; Arc15 (an Arp2/3 complex

subunit), Sac6 (fimbrin), and Ark1 (GAK/AAK) as representative actin module proteins; and Rvs167 (amphiphysin) as a representative scission module protein. Movies of these query proteins yielded new information about every stage of the CME pathway.

A combination of established and custom MATLAB scripts was used to monitor recruitment of individual fluorescently tagged proteins to CME sites. CME sites are smaller than the diffraction limit of fluorescence microscopy, so they appear as ~200 nm diameter spots in our movies. Figure 1B depicts a representative montage of an endocytic site. In this case, the GFP-tagged query protein Las17, the yeast WASP, arrives before the reference protein Abp1-RFP. Both proteins then disappear as the endocytic pit internalizes and leaves the TIRFM field (See also Video 1). We used the cmeAnalysis MATLAB package to automatically track all of the endocytic sites in many fields of yeast cells (Aguet et al., 2013). We then used custom MATLAB scripts to: identify and associate colocalized green and red spots, reject CME sites that were too close to one another to resolve independently, and extract background-subtracted fluorescence intensities for each fluorescence channel at each site (See Materials and Methods for full details). Using our software, we tracked individual endocytic sites from their initiation to their disappearance and extracted time-resolved fluorescence intensity data for each channel (Figure 1B-C).

Our systematic imaging data set provides independent support for the previously proposed recruitment order for CME proteins while providing important additional mechanistic insights. We generated plots of fluorescence intensity vs. time for each fluorescently-tagged protein at each tracked CME site and recorded lifetimes, maximum fluorescence intensities, and the delay between query protein arrival and reference protein arrival (Figure 1C). When we ordered the proteins using our time to reference protein

arrival data, we recapitulated the previously deduced recruitment order (Figure 1D – F, Supplementary Tables 2, 3, and 4). First, our plots show that all early arriving proteins (Ede1, Syp1, Pal1, Hrr25, and Apl1) arrive at CME sites at about the same time when imaged with reference to Ede1-RFP (Figure 1D, Carroll et al., 2012). When imaged with reference to Sla1-mCherry, Ede1 appears to be the earliest arriving protein, although this is likely due to Ede1 being the brightest of the group (Figure 1E, also see Figure 1 Supplement 1A). Finally, our dataset using Abp1 as a reference protein recapitulates the canonical timeline of the CME pathway, an ordering which was previously established only through painstaking sequential rounds of two-color imaging by several groups across many studies (Figure 1F, see Lu et al., 2016 for review). Even fine-grained details are borne out in these plots. For example, the actin assembly factor Arc15-GFP (a component of the Arp2/3 complex) precedes the actin-binding protein Sac6-GFP at CME sites, and Sac6-GFP is followed closely by Ark1-GFP, a kinase recruited to CME sites by actin binding proteins (Figure 1F, Cope et al., 1999). Our ability to recapitulate fine-grained differences in timing gave us confidence to draw new conclusions from our dataset.

Maximum intensity and lifetime measurements also recapitulate trends from the literature. While we did not calibrate fluorescence intensity to count molecules, relative fluorescence intensities we measured are in agreement with those reported previously (Figure 1 Supplement 1A, Supplementary Tables 5, 6, and 7; Picco et al., 2015; Sun et al., 2019). The median lifetimes we measured are also in general agreement with published results (Figure 1 Supplement 1B, Supplementary Tables 8, 9, and 10, Carroll et al., 2012; Kaksonen et al., 2005, 2003; Lu et al., 2016; Peng et al., 2015a; Stimpson et al., 2009). The instances in which our data deviate slightly from the literature are likely due to the

exponential decay of TIRFM illumination with distance from the coverslip (Axelrod, 1989). We undercounted Arc15 slightly, most likely due to the actin network extending further from the coverslip than other endocytic components we imaged. Our recorded lifetimes are also systematically slightly lower than those previously reported, likely due to a failure to record the final moments of each CME event when the invagination/vesicle is moving out of the TIRFM field. Despite these minor artifacts, trends within our systematic TIRFM dataset are concordant with the published literature, empowering our deeper analysis, described below.

One unexpected result from our initial analysis of CME protein dynamics is the amount of variability in our measurements (Figure 1D-F, Figure 1 Supplement 1A-B). Budding yeast CME has canonically been described as being highly regular, particularly during the late stages (Kaksonen et al., 2006; Stimpson et al., 2009; Sun et al., 2015). However, our dataset made us question this characterization. One measure of variability is the coefficient of variation (CV), the ratio of the standard deviation to the mean (Reed et al., 2002). Our data confirm that the earlier stages of CME (CV: ~0.5) are more variable then the later stages, but we nevertheless detected considerable variability during the later stages of the process (CV: ~0.3, See Supplementary Tables 8, 9, and 10). Despite repeated characterization of CME as being "highly regular" in the literature, our CV values appear consistent with previously reported data (Kaksonen et al., 2005, 2003; Sun et al., 2006, where CV values can be estimated from plots of mean/standard deviation). We exploited this previously underappreciated variability to gain new systems-level insights into the mechanisms of CME.

Quantitative evidence for a regulatory transition point in the clathrin-mediated endocytosis pathway

Analysis of paired lifetime and intensity data for individual endocytic proteins revealed at least two distinct behaviors for proteins in the CME pathway. Given the highly interconnected nature of protein interactions at CME sites (Holland and Johnson, 2018; Tonikian et al., 2009), one might predict that longer assembly times at endocytic sites would lead to greater abundancies. To test this prediction, we plotted the maximum intensity from each tracked endocytic event for each query protein as a function of its lifetime (Figure 2, Figure 2 Supplement 1), and performed linear regression analyses. The R^2 value of each fit can be interpreted as the percentage of the variability in maximum intensity that can be explained by the variation in lifetime (Glantz et al., 2001). For early endocytic proteins, exemplified by Ede1, lifetime is poorly correlated with abundance, with linear fits yielding low slopes (0.29) and R^2 values (0.05) (Figure 2A, Supplementary Table 11). Late arriving coat proteins and actin associated proteins, exemplified by Las17 and Sac6, show moderate correlations between lifetime and abundance, with higher slopes (0.97 and 0.91 respectively) and better fits (R^2 = 0.21 and 0.1, respectively) (Figure 2B-C, Supplementary Table 11). Finally, proteins involved in scission and disassembly of the endocytic machinery once again have abundancies that are poorly predicted by residence times (Figure 2D, Supplementary Table 11). To summarize the results from our analysis of each CME protein imaged, we generated bar graphs with the height of the bars representing the slope of the fit and the color of the bars representing the R^2 value (Figure 2D, see Figure 2 Supplement 1 for individual plots, Supplementary Table 11 for fit statistics). From these plots, two distinct behaviors for CME proteins emerge. Early arriving proteins and very late arriving proteins have abundancies that are largely independent of

their lifetimes, while components of the endocytic coat and WASP/Myosin module show a stronger correlation between these parameters. Such temporally resolved differences in behavior hint that a shift in CME protein behavior may occur sometime after endocytic site initiation, but prior to actin assembly.

We next investigated interrelationships between the behaviors of different CME proteins. Many previous studies have presented two-color imaging of CME proteins (Kaksonen et al., 2005, 2003). However, previous analyses have typically relied on separating and averaging measurements of the two protein species imaged, so correlations of the lifetime or intensity of one protein imaged with the lifetime or intensity of the other were lost (Kaksonen et al., 2005).

Since some CME proteins have lifetimes that are correlated with their own maximum intensities, and because CME proteins are extensively interconnected through protein-protein interactions, we wondered whether the lifetimes of any of our query proteins would be predictive of the abundancies of our reference proteins. When we plotted the maximum intensity of our reference proteins at each CME event as a function of the lifetime of the corresponding query protein, we once again detected a quantitative transition point within the CME pathway (Figure 3, Figure 3 Supplement 1). Early proteins such as Ede1 have lifetimes that are poorly correlated with the maximum abundance of the CME actin marker Abp1 (Slope = -0.06, R^2 = 0.00, Figure 3A, Supplementary table 12). In contrast, lifetimes of late arriving coat proteins, WASP/Myosin module proteins, and actin binding proteins, exemplified by Las17 and Sac6, are moderately predictive of maximum Abp1 levels (Slopes = 0.96 and 0.70 respectively, R^2 = 0.13 and 0.07 respectively, Figure 3B-C, Supplementary Table 12). Finally, lifetimes of proteins involved in scission and

disassembly are once again relatively less correlated with maximum Abp1 intensity (Figure 3D, Supplementary Table 12). We again summarized the data from our linear fits by making bar graphs with the height of the bars representing the slope of the fit and the color of the bars representing the R^2 value (Figure 3D, see Figure 3 Supplement 1 for individual plots, Supplementary Table 12 for fit statistics). While the lifetimes of the earliest and latest arriving CME proteins are poorly correlated with the abundance of the actin marker Abp1, all proteins of the late coat and WASP/Myosin CME modules have lifetimes that are comparatively more positively correlated with Abp1 abundance (Figure 3D). We interpreted a correlation between query protein behavior and reference protein behavior to indicate shared protein-protein interactions. These data therefore show that a large fraction of the proteins in the CME pathway can be thought of as an extensively interconnected network, but the earliest and latest arriving CME proteins may be less well connected into this network.

To determine how behaviors of individual CME proteins are correlated with progression through the pathway as a whole, we tested whether lifetimes of any of our query proteins are predictive of the lifetimes of our reference proteins. Early proteins, once again exemplified by Ede1, have lifetimes that are well correlated with other early protein lifetimes (slopes ranging from 0.45 – 0.71, R^2 values ranging from 0.21 – 0.55), but poorly correlated with the lifetimes of the late arriving proteins Sla1 and Abp1 (slopes of 0.17 and 0.08 respectively, R^2 values of 0.06 and 0.03 respectively, Figure 4A, Supplementary Tables 13-15). Late arriving coat proteins and proteins of the WASP/Myosin module have lifetimes that are moderately positively correlated to the lifetime of actin assembly as reported by Abp1 (For Las17, a slope of 0.4 and an R^2 value of 0.24, Figure 4B,

Supplementary Table 15). Actin module proteins, such as Sac6, have lifetimes that are well correlated with the lifetime of the actin marker Abp1 (slope = 0.83, R^2 = 0.71, Figure 4C, Supplementary Table 15). All queried early arriving proteins have lifetimes that are well correlated with the lifetime of the early arriving reference protein Ede1 (Figure 4D, Figure 4 Supplement 1, Supplementary Table 13), suggesting that a signal or a stochastic event, the nature of which is currently unknown, may be required to trigger concerted maturation of the early site. However, long lifetimes of early arriving CME proteins are not predictive of the lifetime of any of the later-arriving reference proteins that we tested; our queried early CME proteins have lifetimes that are poorly correlated with both Sla1 and Abp1 lifetimes (Figure 4E-F, Figure 4 Supplements 2-3, Supplementary Tables 14-15). Thus, while behavior of any one early arriving CME protein is predictive of the behavior of the others, the early proteins are molecularly insulated from the proteins in the late part of the CME pathway.

Together, these data indicate that the CME pathway in budding yeast can be thought of as occurring in two, quantitatively recognizable phases. Early arriving proteins initiate CME sites and persist for a variable period of time, but the length of this variable phase is not predictive of events that occur downstream in the pathway. Around the time of Sla2 recruitment, the CME site transitions into a more regular phase. Extensive protein-protein interactions in this phase make progression though this portion of the CME pathway deterministic. The behavior of any one protein predicts the behavior of other proteins in this phase. Sla2 has been classified as an intermediate coat protein (Carroll et al., 2012), and it is indeed “intermediate” by nearly every measure in our data set. Its lifetime is less variable than those of the early proteins, but more variable than the lifetimes of the late

phase proteins (Early protein CV ~0.5, Late protein CV ~ 0.3, Sla2 CV ~0.4. Supplemental Tables 8, 9, and 10). The lifetime of Sla2 is also intermediately correlated with its own abundance, the abundance of Abp1, and the lifetime of Abp1 (Figure 2F, Figure 3F, and Figure 4F). Sla2 may therefore be involved in transitioning from the early phase of CME into the late phase. A previous study from our lab speculated that such a transition point exists based on the variability of the lifetimes of early arriving endocytic proteins, and further suggested that cargo may regulate progression through a transition point to a more regular phase of the process. Having substantiated the existence of this transition point based on an unbiased quantitative imaging approach, we decided to investigate molecular determinants that dictate the rate of maturation from the early phase into the late phase.

Maturation through the CME transition point is faster in cellular regions with concentrated endocytic cargo

Cargo has previously been suggested to influence the maturation rate of individual CME sites (Carroll et al., 2012; Layton et al., 2011). We set out to determine whether cargo influences maturation through tuning the rate of transition from the early phase of CME to the late phase of CME that we detected in our systematic TIRFM experiments.

As an initial strategy for varying the presence of cargo at CME sites, we took advantage of polarized secretion during the budding yeast cell cycle. When mitotically replicating budding yeast are in the small to medium-budded cell cycle stages, exocytic events are localized primarily to the growing bud, whereas exocytic events are redirected toward either side of the bud neck at cytokinesis (Lew and Reed, 1995). Endocytic cargos such as vesicle-associated SNARE proteins must be retrieved from the plasma membrane

by CME following exocytosis (Lewis et al., 2000). Because septin filaments at the bud neck prevent lateral diffusion between the mother and the bud (Takizawa et al., 2000), the polarized pattern of secretion in small-budded cells concentrates CME cargo in the bud relative to the mother.

To determine whether the presence of endocytic cargo influences the rate of transition from the early phase of CME to the late phase, we imaged a representative protein from each respective endocytic phase through the cell cycle. We chose Ede1-GFP as a representative marker of the early phase of CME and Sla1-mCherry as a representative marker of the late phase. During the small- and medium-budded stages of the cell cycle, when cargo is plentiful in the bud but sparse in the mother, we observed considerable polarization of Sla1-mCherry-marked late CME sites without coincident polarization of Ede1-GFP-marked early CME sites (Figure 5A, Video 2). The disparity in polarization diminishes as cells near cytokinesis, when cargoes are more evenly distributed between the mother and bud due to exocytic events occurring on either side of the contractile ring (Figure 5A, Video 2). As cells begin the next cell cycle, Sla1-marked late phase CME sites again become polarized (Figure 5A, Video 2). Based on the observation that early CME sites are depolarized while late CME sites are polarized within the same cell, we concluded that the presence of cargo does not affect the rate of CME site initiation appreciably, but it does increase the proportion of initiated CME sites that mature.

The abundance of early CME sites relative to late CME sites in the mother cells of polarized budding yeast could be explained by the presence of either abortive or stalled CME events in the mother cells. The “extra” Ede1-GFP-marked early sites that we observed could either abort, leading to the dearth of Sla1-marked late CME sites in the mother cells,

or they could mature at a slower rate, also resulting fewer late phase sites. To distinguish between these possibilities, we used a two-step imaging regime to first identify highly polarized and depolarized cells, and to then track the fate of early CME sites in each cell type. First, we collected 5 μm z-stacks (11 slices, 500 nm each) to identify highly polarized cells, defined as small-budded cells with 3 or fewer Sla1-mCherry-marked late CME sites in the mother, and depolarized cells, defined as medium- or large-budded cells with greater than 3 Sla1-mCherry-marked late CME sites in the mother (Figure 5B, left photos). Next, we collected time series in the medial focal plane of the same cells for 4 minutes with an interval of 2 seconds between frames and generated circumferential kymographs along the mother cortex (Figure 5B, right photos, Video 3). Our imaging protocol allowed us to confidently identify highly polarized and depolarized cells and to visualize CME at high temporal resolution in the cells identified.

When we analyzed the fates of individual CME sites in polarized and depolarized cells, we determined that the rate of maturation through the transition point is accelerated by proximity to exocytic sites and/or the cell polarity machinery. Quantification of the ratio of the number of late CME sites to early sites in mothers of highly polarized and depolarized cells confirms the observation that there are significantly more Ede1-GFP-marked early CME sites per Sla1-mCherry-marked late site in mothers of small-budded cells (median ratio of 0.08 vs. 0.44, Figure 5B left photos, Figure 5C). Tracking the fate of every early CME site in the medial focal plane by generating circumferential kymographs failed to reveal any abortive CME events, but it revealed many persistent early sites (Figure 5B right photos, Figure 5D, Video 3). While we could not reliably extract Ede1 lifetimes due to a large fraction of Ede1 puncta being present at the start and end of our movies, we

observed significantly more long-lived Ede1-marked early CME sites in kymographs from mothers in highly polarized cells than from mothers in depolarized cells (21.3% persistent sites compared to 0.3%, 58.7% "partial" sites compared to 34.9%, Figure 5D, see figure legend). This observation suggests that the maturation rate from the early phase of CME to the late phase is slower when a CME site is further from cargo and the cell polarity machinery. When we conducted the same kinds of experiments with two late-phase CME markers, Sla1-GFP and Abp1-RFP, neither the ratio of numbers of puncta nor the lifetimes of these CME markers were sensitive to polarization state (median ratios 0.56 compared to 0.63, Figure 5 Supplement 1A, B, and C). While Abp1 lifetimes differ slightly (by 0.5 s, $p = 0.0247$), the small magnitude of this difference makes it unlikely to be biologically relevant. Based on these observations, we concluded that proximity to cargo and/or polarity machinery accelerates the rate of maturation from the early phase of CME to the late phase, but does not affect the kinetics of late events in CME.

The proximity of cargo, rather than cell cycle stage, appears to dictate maturation rate through the regulatory transition point

To determine whether the differences we observed in CME site maturation rate were due to polarization state or cell cycle stage, we used osmotic shock to reposition CME cargos and cell polarity proteins independent of cell cycle stage. A previous study from our lab used a temperature-sensitive secretion mutant to halt accumulation of endocytic cargo on the plasma membrane and reported increased numbers of long-lived Ede1-GFP-marked CME sites (Carroll et al., 2012). We conducted the converse experiment by redistributing endocytic cargo from the plasma membrane of buds in highly polarized cells to the plasma

membrane of mother cells, testing whether long-lived early phase CME sites could be induced to mature simply though loss of cell polarity and redirection of cargo. Diluting *S. cerevisiae* cells out of media into water has previously been reported to trigger depolarization (Pringle et al., 1989). We found that osmotically shocking highly polarized cells by rapidly diluting them with water caused dispersal of the polarity marker Bem1-GFP (Figure 6A-B). Depolarization also results in redistribution of GFP-Sec4-marked secretory vesicles from a bud-localized distribution to a more uniform one, suggesting that exocytic traffic (and therefore endocytic cargo) is repositioned by this manipulation (Figure 6 Supplement 1A). We therefore used osmotic shock to acutely depolarize cells without influencing the cell cycle.

Forced depolarization through osmotic shock accelerates maturation through the transition point in mothers of small-budded cells. When we examined the CME markers Ede1-GFP and Sla1-mCherry in polarized mothers before and after osmotic shock, we found that the treatment caused Sla1-mCherry sites to depolarize. Ede1-GFP sites were not noticeably affected (Figure 6C). Quantification of the ratio of the number of late phase CME sites to early phase CME sites in these cells reveals a change in ratio reminiscent of the one that occurs naturally during the cell cycle (median ratio changes from 0.09 to 0.43, Figure 6D, see also Figure 5C). To determine whether this transition was caused by a change in the maturation rate of CME sites, we examined Ede1-GFP tracks in circumferential kymographs made from cells before and after osmotic shock (Figure 6E). We observed a significant decrease in the proportion of long-lived early CME sites upon osmotic shock, suggesting that early phase CME sites mature to the late, regular phase more quickly (from 22.9% persistent sites to 0.2%, 54.3% partial sites compared to 38.6%, Figure 6F). Interestingly,

the apparent shortening of Ede1-GFP lifetimes by osmotic shock does not extend to late phase CME proteins. While the ratio of the number of Abp1-RFP to Sla1-GFP puncta was unchanged, both Sla1-GFP and Abp1-RFP lifetimes were significantly increased upon osmotic shock (median lifetimes of 22 and 10 s, respectively, before osmotic shock and 34 and 13 s, respectively, after. Figure 6 Supplement 1B-E). Lengthening of Sla1-GFP and Abp1-RFP lifetimes is likely due to a mechanical burden on membrane invagination/internalization caused by increased turgor pressure in hypotonic solution (Aghamohammadzadeh and Ayscough, 2009; Boulant et al., 2011; Hassinger et al., 2017). With these data, we demonstrated that proximity to cargo and/or the polarity machinery accelerates CME site maturation from the early phase to the late phase of the pathway, even as vesicle internalization itself is slowed. The transition point we identified can therefore be considered a cargo checkpoint.

The mechanism of cargo sensing within the CME pathway remains unclear. We considered one candidate cargo sensing molecule, the casein kinase Hrr25. A previous study from our lab identified several proteins from the early phase of CME as Hrr25 substrates (Peng et al., 2015a). In the same study, cells lacking Hrr25 were found to have fewer Sla1 sites, while cells overexpressing Hrr25 had more Sla1 sites. We wondered whether this effect could be due to modulation of the rate of transit through the cargo checkpoint. While depletion of Hrr25 using an auxin inducible degron (AID, Nishimura et al., 2009) causes a growth defect detectable at low temperatures (Figure 6 Supplement 2A), acutely-induced and nearly complete degradation of the kinase causes only a moderate increase in the fraction of long-lived Ede1-GFP sites in small-budded mothers (Figure 6 Supplement 2B-D). Conversely, overexpression of Hrr25 using a β-estradiol induced

overexpression system (McIsaac et al., 2011) causes only a moderate increase in the fraction of short-lived Ede1-GFP sites in mothers of small-budded cells (Figure 6 Supplement 2E-F). While the mechanism of cargo sensing in the CME pathway remains unclear, these findings suggest that the casein kinase Hrr25 may contribute to the transition.

The regulatory transition point occurs between recruitment of the intermediate coat proteins and late coat proteins

Since a representative CME protein from before the regulatory transition point (Ede1) was not significantly polarized in small-budded cells but a late phase CME protein (Sla1) was (Figure 5), we used this difference in CME protein distribution as an assay to pinpoint the time of the regulatory transition point in the CME pathway. We recorded Z-stacks of proteins from the early, early coat, intermediate coat, and late coat using either epifluorescence microscopy or spinning disc microscopy (depending on how well we could distinguish CME puncta above background noise). The early proteins Syp1 and Hrr25, the early coat proteins Apl1 and Pal1, and the intermediate coat proteins Sla2, Ent1, and Ent2 all display distributions similar to that of Ede1: in highly polarized cells with few Sla1-mCherry-marked late CME sites, we nevertheless observed many puncta of these query proteins, placing them upstream of the transition point (median ratios of 0.14 vs. 0.59 (Syp1), 0.09 vs. 0.49 (Sla2), 0.16 vs. 0.79 (Ent2), Figure 7A-B, Figure 7 Supplement 1). The late coat marker Pan1, on the other hand, polarizes with Sla1-mCherry-marked late CME sites (median ratio of 0.62 vs. 0.64, Figure 7A-B). These data indicate that the transition

1 point in the CME pathway occurs after recruitment of the intermediate coat module but

2 before recruitment of the late coat proteins Pan1 and Sla1.

Discussion

Despite identification of dozens of proteins involved in CME through decades of research, how progression through this pathway is regulated is poorly understood. In this study, we conducted systematic imaging experiments of CME in budding yeast with the goal of revealing new regulatory principles. Previous studies used two-color imaging to describe a protein recruitment cascade at CME sites; however, these studies typically analyzed the recruitment dynamics of each protein independently, therefore losing information about how the behavior of one protein is correlated with the behavior of another at individual endocytic sites. To uncover inter-relationships in the behavior of individual components of the CME machinery, we performed quantitative analysis of the pair-wise recruitment and abundance behavior of CME proteins at >17,000 endocytic sites.

Our data set revealed more variation in the behavior of individual proteins in the budding CME pathway than had previously been appreciated. CME has been described as a highly regular molecular pathway. The ordered arrival of CME proteins at endocytic sites is roughly conserved from yeasts to humans and is nearly invariant (Doyon et al., 2011; Kaksonen et al., 2005, 2003; Sun et al., 2019; Taylor et al., 2011). While the initial steps of CME were known to occur with variable timing, the timing of the late steps of the pathway had been considered to be remarkably regular (Kaksonen et al., 2006). Previous studies even used lifetimes of late phase CME proteins as readouts for endocytic efficiency (Kaksonen et al., 2005). While our data confirm that the early stages of CME occur with more variable timing than the late stages, we were surprised to nevertheless observe variability even in what has previously been considered the “regular phase” of the process. We took advantage of this previously underappreciated variability in timing to gain new

insights into the CME pathway by looking for covariation in the pair-wise behavior of endocytic proteins.

Our analysis suggests that a full complement of early arriving CME proteins is present at each endocytic site at initiation. Each early arriving endocytic protein has been reported to have a variable lifetime (Carroll et al., 2012, 2009; Newpher et al., 2005; Peng et al., 2015a; Stimpson et al., 2009). However, the implication of this variability was previously unknown. One possible interpretation was that long-lived early CME sites represent sites that are incompletely assembled, potentially lacking some component of the early or early coat module. Another possibility was that the early proteins assemble fully but that maturation to the next phase of the pathway is stalled due to an inhibitory checkpoint signal. Our pair-wise analysis of the lifetimes of each early arriving protein and Ede1 shows that they are well correlated. This correlation is consistent with the possibility that CME proteins assemble at the nascent sites in a coordinated manner, but that advancement to the next phase awaits release of a checkpoint.

Analyses of correlations between the behaviors of different pairs of proteins at individual CME sites also reveal two quantitatively separable stages, substantiating the existence of a regulatory transition point in the CME pathway (Carroll et al., 2012, Figure 8A). This conclusion is based on the loss of correlation of lifetimes and intensities for proteins spanning a specific step in the pathway. While lifetimes of early arriving proteins are predictive of one another (for example, a plot of Ede1 lifetime vs. Syp1 lifetime yields a linear fit with a slope of 0.65 and an R^2 of 0.35), in no case does the behavior of an early arriving protein strongly correlate with the behavior of a late arriving protein (for example, a plot of Ede1 lifetime vs. Abp1 lifetime yields a linear fit with a slope of 0.08 and an R^2 of

0.03). Conversely, lifetimes of late arriving proteins are fairly good predictors of the maximum intensity of the endocytic actin reporter Abp1 (Slopes ranging from 0.46 to 0.96). The striking correlations within groups of proteins recruited early or late, but not between these groups, is consistent with the notion that robust protein interaction networks are at play during CME: an early complex of proteins establishes endocytic sites and a late complex mediates membrane invagination and vesicle scission (Figure 8A). The poor correlation between the lifetimes and intensities of these two networks likely indicates that there are fewer molecular links between the two networks than within each respective network. Since the behavior of proteins in the early and late phases have behaviors that are predictive of behaviors of other proteins in the same phase, but not the other phase, CME initiation and internalization can be thought of as two separable processes.

Through observation of CME site composition and dynamics while directionality of polarized yeast growth changed naturally in a programmed manner through the cell cycle, and through artificial perturbation of cell polarity, we obtained evidence in support of the conclusion that progression from the early to the late phase of CME is controlled by cargo (Figure 8A). Although it is formally possible that the cell polarity machinery composed of proteins such as Cdc42 and Cdc24 might directly trigger the transition from the early to the late phase of CME, we favor the possibility that cargo plays a direct role. This is in part because CME would be more efficient with a cargo sensing mechanism and in part because our earlier studies (Carroll et al., 2012) showed that CME stalls when secretion is blocked even though cell polarity is maintained. These experiments also suggest that a portion of the variability observed for early arriving endocytic proteins can be explained by

differences in the polarization state of the cells analyzed. Thus, in *S. cerevisiae*, cargo-mediated regulation of CME progression occurs through widespread endocytic stalling, rather than abortion, in the absence of cargo.

While the specific molecular mechanism of this proposed cargo checkpoint is incompletely understood, several intriguing possibilities provide exciting avenues for further research. Importantly, several studies have suggested that a cargo checkpoint might regulate progress through the mammalian CME pathway (Liu et al., 2010; Loerke et al., 2009; Mettlen et al., 2010; Puthenveedu and von Zastrow, 2006). A recent reconstitution study of mammalian CME suggests that clathrin continually assembles and disassembles during the early stage of the process, with cargo binding stabilizing membrane-associated clathrin structures (Chen et al., 2019). Fluorescently-tagged early arriving CME proteins in budding yeast are also known to fluctuate in intensity, suggesting that such a dynamic proofreading mechanism may be evolutionarily conserved (Carroll et al., 2012). Cargo sensing might involve post-translational modification. We provided evidence that the casein kinase Hrr25 may play a role in progression of CME from the cargo collection phase to the internalization phase. In addition, ubiquitination has also been suggested to play a role in CME (Weinberg and Drubin, 2014). One attractive possibility is that early arriving CME proteins dynamically bind and unbind nascent endocytic sites until cargo binding induces a conformational change, facilitating post-translational modification and maturation.

Because representative early phase CME proteins do not appear polarized in budding yeast while representative late phase CME proteins do, we assessed polarization state of more proteins to precisely define which CME proteins are present on either side of

the transition point in the CME pathway. We found that sites containing Ede1, Syp1, Hrr25, the AP-2 complex, Pal1, Sla2, and the epsins all behaved similarly in that they are found both proximal and distal to sites of polarized growth. In contrast, sites containing Pan1 and Sla1, late coat proteins, are highly polarized (Figure 8A). Intriguingly, several previous studies have suggested a transition at a similar point on the CME timeline based on very different types of observations. Acute depletion of late coat proteins Pan1 and End3, the first proteins to arrive at CME sites after Sla2 and the epsins, leads to arrest of early endocytic sites on the plasma membrane and aberrant assembly of the late endocytic proteins including the actin cytoskeleton in the cytoplasm (Sun et al., 2015). Thus recruitment of these late coat proteins is likely the crucial step in transitioning from the early phase to the late phase of CME. Conversely, deletion of 7 early arriving proteins (Syp1, Ede1, Apl1, Pal1, Pal2, Yap1801, and Yap1802) leads to defects in cargo collection but does not halt endocytosis itself (Brach et al., 2014). Loss of a "checkpoint" protein that halts progress in endocytosis in the absence of cargo may be permissive for progress in the CME pathway if that protein does not perform an additional, essential CME function. One of these seven early arriving proteins might therefore be responsible for detecting cargo in a nascent endocytic pit and releasing the block on Pan1/End3 recruitment.

Together, the data we collected and analyzed in this study suggest a simple conceptual model to explain placement of endocytic internalizations (Figure 8B). Endocytic sites are initiated widely across the plasma membrane. However, in the absence of cargo, they mature to the internalization phase slowly due to an unsatisfied cargo checkpoint, rather than aborting in the absence of cargo, as has been reported previously (Ehrlich et al., 2004; Liu et al., 2010; Loerke et al., 2009; Mettlen et al., 2010). Localized delivery of

endocytic cargos via exocytosis triggers localized maturation of CME sites through release of the cargo checkpoint. This interpretation represents an attractive explanation for the decades-old observation that "actin patches" (late CME sites) are polarized in small and medium budded *S. cerevisiae* cells (Adams and Pringle, 1984). Because secretion is directed primarily to the bud while it is growing (Field and Schekman, 1980), concentrated endocytic cargos in the bud trigger local maturation of endocytic sites through the cargo checkpoint, after which actin assembles.

Materials and methods

Strains and yeast husbandry

The strains used in this study are listed in Supplementary Table 1. All budding yeast strains were derived from the wild-type diploid DDY1102 and propagated using standard techniques (Amberg et al., 2005). C-terminal fluorescent protein fusions were constructed specifically for this study or for earlier studies, as indicated in Table 1, as described previously (Longtine et al., 1998).

Live-cell imaging

Cells were grown to mid log phase in imaging media (synthetic minimal media supplemented with Adenine, L-Histidine, L-Leucine, L-Lysine, L-Methionine, Uracil, and 2% glucose), then adhered to coverslips coated with 0.2 mg/ml Concanavalin A.

TIRFM imaging was performed on a Nikon Eclipse Ti2 inverted microscope with a Nikon CFI60 60× 1.49 numerical aperture (NA) Apo oil immersion TIRFM objective and a Hamamatsu Orca-Flash 4.0 V2 sCMOS camera. GFP and RFP/mCherry were excited using 488- and 561-nm lasers and detected using a Chroma HC TIRFM Quad Dichroic (C-FL TIRF Ultra Hi S/N 405/488/561/638) and Chroma HC Quad emission filters BP 525/550 and BP 600/650, respectively. Channels were acquired sequentially. The system was controlled with Nikon Elements software and maintained at 25˚C by an OkoLab environmental chamber. Frames were separated by 1 sec.

Epifluorescence imaging was carried out on a Nikon Eclipse Ti inverted microscope with a Nikon 100x 1.4 NA Plan Apo VC oil immersion objective and an Andor Neo 5.5 sCMOS camera. GFP and RFP/mCherry fluorescence were excited using a Lumencore

Spectra X LED light source with 550/15 nm and 470/22 nm excitation filters. For two-color imaging, channels were acquired sequentially using an FF-493/574-Di01 dual pass dichroic mirror and FF01-524/628-25 dual pass emission filters (Semrock, Rochester, NY). The system was controlled with Nikon Elements software and maintained at 25˚C by an environmental chamber (In Vivo Scientific, St. Louis, MO).

Spinning disc confocal microscopy was carried on a Nikon Eclipse Ti inverted microscope with a Nikon 100x 1.45 NA Plan Apo λ oil immersion objective, an Andor IXon X3 EM-CCD camera and Andor CSU-X spinning disc confocal equipment. GFP fluorescence was excited using a 488 nm laser and detected with a Chroma 535/20 nm emission filter (Bellows Falls, VT). mCherry fluorescence was excited using a 565 nm laser and detected with a Chroma 605/52 nm emission filter. The system was controlled with Nikon Elements software. Imaging was conducted at room temperature (~23˚C).

Osmotic shock experiments

For osmotic shock experiments, cells were adhered to Concanavalin A coated coverslips for live cell imaging, but overlaid with only 250 μL imaging media. Osmotic shock was achieved through rapid addition of 4 mL of sterile water or 4 mL imaging media as a control.

Auxin depletion experiments

For auxin depletion experiments, 500 μM 3-indoleacetic acid (auxin, Sigma) was prepared freshly in DMSO and added to standard *S. cerevisiae* growth media. As depletion is most efficient in slightly acidic media, YPD media used in growth assays was supplemented with

0.1 M potassium phosphate buffer (pH 6.2). Liquid imaging media was sufficiently acidic without buffering.

For growth comparisons in the presence of auxin, mid log phase starter cultures were diluted to an OD_{600} of 0.1, 0.02, and 0.004, spotted on plates with and without added auxin, and grown for 48 hours at 18° C and 25° C.

For immunoblot and live cell imaging analysis, auxin was added directly to mid log phase cultures in imaging media. The cultures were then incubated at room temperature (~23° C) for the indicated time interval, after which they were either imaged by epifluorescence microscopy or processed for immunoblot analysis.

β-estradiol-induced overexpression experiments

Hormone-induced overexpression of Hrr25 was carried out essentially as in Peng et al. 2015a. Briefly, 50 mM β-estradiol (Sigma) was prepared freshly in DMSO and added to mid log phase cultures in imaging media. The cultures were then incubated at 25° C for the indicated time interval, after which they were either imaged by epifluorescence microscopy or processed for immunoblot analysis.

Immunoblot analysis

Cells were grown to mid log phase in the appropriately supplemented imaging media, harvested by centrifugation, washed with water, and lysed by bead beating in a lysis buffer with 5 mM Tris-HCl pH 8, 5 mM EDTA pH 8, and 15% Trichloroacetic acid (TCA). The TCA precipitate was then washed with ice-cold acetone and resuspended in Tris/urea sample buffer (62.5 mM Tris pH 6.8, 3 M urea, 1% sodium dodecyl sulfate, 5% beta

mercaptoethanol, 0.05% bromophenol blue). Extracts were separated electrophoretically on 10% polyacrylamide gels and transferred to nitrocellulose. Membranes were blocked with 5% milk and probed with the one or more of the following antibodies (indicated): a mouse monoclonal antibody against the V5 epitope tag (Invitrogen), mouse monoclonal antibody clone 9E10 against a 13-myc tag (prepared from hybridoma supernatant (Lewellyn et al., 2015)), a mouse antibody raised against Hrr25 (Abmart, Peng et al., 2015b), or a mouse monoclonal antibody against Pgk1 (459250; Novex, Winston-Salem, NC). Membranes were then incubated with secondary antibodies conjugated to infrared fluorophores (Li-Cor Biosciences inc., Lincoln, NE). Bands were visualized using an Odyssey infrared imaging system (Li-Cor Biosciences).

Image and data analysis

Tracking of endocytic sites was performed using the MATLAB package cmeAnalysis (Aguet et al., 2013). The red and green channels for each movie were tracked independently, and the centroid position over time for each site determined. These data were used as input in custom MATLAB scripts that associated colocalized tracks in the red and green channels while rejecting sites that appeared within 350 nm of one another (Hong et al., 2015). The fluorescence intensity for each spot was calculated as an integrated intensity within a circular region with a diameter of 7 pixels (756 nm), centered at the spot position determined by cmeAnalysis. The background fluorescence was calculated as the average fluorescence intensity of an annulus 2 pixels (216 nm) wide surrounding the circular region used to calculate the spot intensity.

Custom MATLAB scripts were then used to clean our dataset by rejecting tracks that fall into several categories: sites with a low signal-to-noise (brightness not significantly above background, Hong et al., 2015) were excluded from further analysis. Tracks that began or terminated within 5 frames of the beginning or end of the movie were excluded so that only complete tracks were kept for analysis. Sites whose calculated background-subtracted intensity went below −0.25× the maximum intensity were excluded to prevent abnormally high background or presence of nearby sites from affecting intensity measurements. Finally, outliers in spot lifetime, fluorescence intensity, time to arrival, and time to disappearance (defined as more than 1.5× the interquartile distance from the median value) were also excluded. This was done to exclude erroneous traces in which two distinct tracks had been inadvertently linked, where two sites overlapped and thus were substantially brighter, as well as erroneous putative colocalizations. While these analyses were blind to cell cycle stage, long-lived early sites in polarized mothers represented a small fraction of the final data set owing to the requirement for association of query protein tracks with reference protein tracks and exclusion of incomplete tracks.

GFP maximum fluorescence intensity and the lifetimes and maximum intensities of the red reference proteins were fit to the lifetimes of the GFP-tagged query proteins via simple linear regression. To compare the slopes of the fit across GFP-tagged proteins with differing brightnesses and lifetimes, the data were first normalized by dividing by their respective medians, which does not change the R^2 of the fit.

Analysis of the influence of cargo on CME site maturation was carried out using Fiji software (National Institutes of Health, Bethesda, MD). For quantification of Ede1-GFP turnover, circumferential kymographs were generated by drawing a line of width 5 pixels

around the circumference of each cell. For quantification of Sla1-GFP and Abp1-RFP patch lifetimes, radial kymographs were generated using a custom Fiji macro that generates a kymograph at every radius around a circle in 2-degree increments. The lifetimes of the first 5 kymographs generated were measured to avoid bias. For intensity profile analysis of Bem1-GFP, intensity profiles were normalized to cell length and averaged using a Fiji plugin provided by C. Brownlee (Brownlee and Heald, 2019). Exact numbers of cells and CME sites measured are described in the figure legends.

Figure preparation

For figure panels and movies, individual cells were cropped, background fluorescence was uniformly subtracted from the image stack, and photo bleaching was fit to a linear decay function and corrected in Fiji. Look up tables used for display are linear. Plots were generated in MATLAB or Prism 8 (GraphPadSoftware, San Diego, CA). Figures were assembled in Adobe illustrator Creative Cloud 2019.

Reproducibility of experiments

All experimental results presented were replicated in at least three distinct experiments to ensure reproducibility.

For TRIFM imaging experiments, endocytic sites from each of the dozens of cells in several fields of view were tracked simultaneously. As the results from each dataset were indistinguishable, they were pooled for further analysis. The number of tracked spots for each protein pair is presented in Supplementary Tables 2-10. Statistical analysis was conducted in MATLAB.

For epifluorescence and confocal fluorescence imaging experiments, multiple cells from each replicate were analyzed. As data from different replicates were indistinguishable, they were pooled for statistical analysis. The specific number of cells analyzed is indicated in each figure legend. Statistical analysis was conducted in Prism 8.

Data and code availability

The data and code described can be found at the following links:
https://github.com/DrubinBarnes/Pedersen_Hassinger_Marchando_Drubin_CME_Manuscript_2019
https://drive.google.com/drive/folders/1I-v1BiOq0la4_07y74EOlG6_6JexlqW4

Acknowledgements

We thank Yui Iwamoto for critically reading the manuscript. We are grateful to Tony Bretscher for providing the GFP-Sec4 yeast strain and Michelle Lu for providing the Bem1-GFP yeast strain. Spinning disc confocal microscopy was conducted at the University of California, Berkeley Cancer Research Laboratory Molecular Imaging center, supported by the Gordon and Betty Moore foundation. We would like to thank H. Aaron and F. Ives for their microscopy training and assistance. This research was conducted with US Government support, under and awarded by Department of Defense, Air Force Office of Scientific Research, National Defense Science and Engineering Graduate Fellowship 32 CFR 168a (to J.E.H.); National Institutes of Health Grant R35GM118149 (to D.G.D.).

Author Contributions

R.T.A. Pedersen, J.E. Hassinger, and D.G. Drubin conceived of the experiments. R.T.A. Pedersen and P. Marchando generated the reagents. R.T.A. Pedersen, J.E. Hassinger, and P. Marchando performed the experiments, and analyzed the data. R.T.A. Pedersen, J.E. Hassinger, and D.G. Drubin wrote the manuscript. D.G. Drubin secured funding.

Competing interests

The authors declare no competing interests.

References

Adams AE, Pringle JR. 1984. Relationship of actin and tubulin distribution to bud growth in wild- type and morphogenetic-mutant *Saccharomyces cerevisiae*. *J Cell Biol* **98**:934–945. doi:10.1083/jcb.98.3.934

Aghamohammadzadeh S, Ayscough KR. 2009. Differential requirements for actin during yeast and mammalian endocytosis. *Nat Cell Biol* **11**:1039–1042. doi:10.1038/ncb1918

Aguet F, Antonescu CN, Mettlen M, Schmid SL, Danuser G. 2013. Advances in analysis of low signal-to-noise images link dynamin and AP2 to the functions of an endocytic checkpoint. *Dev Cell* **26**:279–291. doi:10.1016/j.devcel.2013.06.019

Amberg DC, Burke DJ, Strathern JN. 2005. Methods in Yeast Genetics: A Cold Spring Harbor Laboratory Course Manual, 2005 Edition, A Cold Spring Harbor Laboratory Course Manual.

Axelrod D. 1989. Total Internal Reflection Fluorescence Microscopy. *Methods Cell Biol* **30**:245–270.

Bitsikas V, Corrêa IR, Nichols BJ. 2014. Clathrin-independent pathways do not contribute significantly to endocytic flux. *Elife* **3**:1–26. doi:10.7554/elife.03970

Boulant S, Kural C, Zeeh J-C, Ubelmann F, Kirchhausen T. 2011. Actin dynamics counteract membrane tension during clathrin-mediated endocytosis. *Nat Cell Biol* **13**:1124–31. doi:10.1038/ncb2307

Brach T, Godlee C, Moeller-Hansen I, Boeke D, Kaksonen M. 2014. The initiation of clathrin-mediated endocytosis is mechanistically highly flexible. *Curr Biol* **24**:548–54. doi:10.1016/j.cub.2014.01.048

Bradford MK, Whitworth K, Wendland B. 2015. Pan1 regulates transitions between stages of clathrin-mediated endocytosis. *Mol Biol Cell* **26**:1371–1385. doi:10.1091/mbc.E14-11-1510

Brownlee C, Heald R. 2019. Importin α Partitioning to the Plasma Membrane Regulates Intracellular Scaling. *Cell* **176**:805-815.e8. doi:10.1016/j.cell.2018.12.001

Carroll SY, Stimpson HEM, Weinberg J, Toret CP, Sun Y, Drubin DG. 2012. Analysis of yeast endocytic site formation and maturation through a regulatory transition point. *Mol Biol Cell* **23**:657–668. doi:10.1091/mbc.E11-02-0108

Carroll SY, Stirling PC, Stimpson HEM, Gießelmann E, Schmitt MJ, Drubin DG. 2009. A Yeast Killer Toxin Screen Provides Insights into A/B Toxin Entry, Trafficking, and Killing Mechanisms. *Dev Cell* **17**:552–560. doi:10.1016/j.devcel.2009.08.006

Chen Y, Yong J, Martinez-sanchez A, Yang Y, Wu Y, De Camilli P, Fernández-busnadiego R, Wu M. 2019. Dynamic Instability of Clathrin Assembly Provides Proofreading Control for Endocytosis. *J Cell Biol*. doi:10.1083/jcb.201804136

Cocucci E, Aguet F, Boulant S, Kirchhausen T. 2012. The first five seconds in the life of a clathrin-coated pit. *Cell* **150**:495–507. doi:10.1016/j.cell.2012.05.047

Cope MJ, Yang S, Shang C, Drubin DG. 1999. Novel protein kinases Ark1p and Prk1p associate with and regulate the cortical actin cytoskeleton in budding yeast. *J Cell Biol* **144**:1203–18.

Daste F, Walrant A, Holst MR, Gadsby JR, Mason J, Lee JE, Brook D, Mettlen M, Larsson E, Lee SF, Lundmark R, Gallop JL. 2017. Control of actin polymerization via the coincidence of phosphoinositides and high membrane curvature. *J Cell Biol* **216**:3745–3765.

doi:10.1083/jcb.201704061
Doyon JB, Zeitler B, Cheng J, Cheng AT, Cherone JM, Santiago Y, Lee AH, Vo TD, Doyon Y, Miller JC, Paschon DE, Zhang L, Rebar EJ, Gregory PD, Urnov FD, Drubin DG. 2011. Rapid and efficient clathrin-mediated endocytosis revealed in genome-edited mammalian cells. *Nat Cell Biol* **13**:331–337. doi:10.1038/ncb2175
Ehrlich M, Boll W, Van Oijen A, Hariharan R, Chandran K, Nibert ML, Kirchhausen T. 2004. Endocytosis by random initiation and stabilization of clathrin-coated pits. *Cell* **118**:591–605. doi:10.1016/j.cell.2004.08.017
Field C, Schekman R. 1980. Localized secretion of acid phosphatase reflects the pattern of cell surface growth in *Saccharomyces cerevisiae*. *J Cell Biol* **86**:123–128. doi:10.1083/jcb.86.1.123
Glantz SA, Slinker BK, Neilands TB. 2001. Primer of Applied Regression and Analysis of Variance, 3rd ed. New York, NY: McGraw-Hill.
Godlee C, Kaksonen M. 2013. From uncertain beginnings: Initiation mechanisms of clathrin-mediated endocytosis. *J Cell Biol* **203**:717–725. doi:10.1083/jcb.201307100
Hassinger JE, Oster G, Drubin DG, Rangamani P. 2017. Design principles for robust vesiculation in clathrin-mediated endocytosis. *Proc Natl Acad Sci U S A* **114**:E1118–E1127. doi:10.1073/pnas.1617705114
Henne WM, Boucrot E, Meinecke M, Evergren E, Vallis Y, Mittal R, McMahon HT. 2010. FCHo proteins are nucleators of Clathrin-Mediated endocytosis. *Science* **328**:1281–1284. doi:10.1126/science.1188462
Holland DO, Johnson ME. 2018. Stoichiometric balance of protein copy numbers is measurable and functionally significant in a protein-protein interaction network for yeast endocytosis. *PLoS Comput Biol* **14**:1–34. doi:10.1371/journal.pcbi.1006022
Hong SH, Cortesio CL, Drubin DG. 2015. Machine-Learning-Based Analysis in Genome-Edited Cells Reveals the Efficiency of Clathrin-Mediated Endocytosis. *Cell Rep* **12**:2121–2130. doi:10.1016/j.celrep.2015.08.048
Johansen J, Alfaro G, Beh CT. 2016. Polarized Exocytosis Induces Compensatory Endocytosis by Sec4p-Regulated Cortical Actin Polymerization. *PLoS Biol* **14**:1–24. doi:10.1371/journal.pbio.1002534
Kaksonen M, Roux A. 2018. Mechanisms of clathrin-mediated endocytosis. *Nat Rev Mol Cell Biol* **19**:313–326. doi:10.1038/nrm.2017.132
Kaksonen M, Sun Y, Drubin DG. 2003. A pathway for association of receptors, adaptors, and actin during endocytic internalization. *Cell* **115**:475–87.
Kaksonen M, Toret CP, Drubin DG. 2006. Harnessing actin dynamics for clathrin-mediated endocytosis. *Nat Rev Mol Cell Biol* **7**:404–414. doi:10.1038/nrm1940
Kaksonen M, Toret CP, Drubin DG. 2005. A modular design for the clathrin- and actin-mediated endocytosis machinery. *Cell* **123**:305–20. doi:10.1016/j.cell.2005.09.024
Layton AT, Savage NS, Howell AS, Carroll SY, Drubin DG, Lew DJ. 2011. Modeling vesicle traffic reveals unexpected consequences for Cdc42p-mediated polarity establishment. *Curr Biol* **21**:184–194. doi:10.1016/j.cub.2011.01.012
Lew DJ, Reed SI. 1995. Cell cycle control of morphogenesis in budding yeast. *Curr Opin Genet Dev* **5**:17–23. doi:10.1016/S0959-437X(95)90048-9
Lewellyn EB, Pedersen RTA, Hong J, Lu R, Huntly M, Drubin DG. 2015. An Engineered Minimal WASP-Myosin Fusion Protein Reveals Essential Functions for Endocytosis. *Dev Cell* **35**:281–294. doi:10.1016/j.devcel.2015.10.007

Lewis MJ, Nichols BJ, Prescianotto-Baschong C, Riezman H, Pelham HRB. 2000. Specific Retrieval of the Exocytic SNARE Snc1p from Early Yeast Endosomes. *Mol Biol Cell* **11**:23–38. doi:10.1091/mbc.11.1.23

Liu AP, Aguet F, Danuser G, Schmid SL. 2010. Local clustering of transferrin receptors promotes clathrin-coated pit initiation. *J Cell Biol* **191**:1381–1393. doi:10.1083/jcb.201008117

Loerke D, Mettlen M, Yarar D, Jaqaman K, Jaqaman H, Danuser G, Schmid SL. 2009. Cargo and Dynamin Regulate Clathrin-Coated Pit Maturation. *PLoS Biol* **7**:e1000057. doi:10.1371/journal.pbio.1000057

Longtine MS, McKenzie a, Demarini DJ, Shah NG, Wach a, Brachat a, Philippsen P, Pringle JR. 1998. Additional modules for versatile and economical PCR-based gene deletion and modification in *Saccharomyces cerevisiae*. *Yeast* **14**:953–61. doi:10.1002/(SICI)1097-0061(199807)14:10<953::AID-YEA293>3.0.CO;2-U

Lu R, Drubin DG. 2017. Selection and stabilization of endocytic sites by Ede1, a yeast functional homologue of human Eps15. *Mol Biol Cell* **28**:567–575. doi:10.1091/mbc.E16-06-0391

Lu R, Drubin DG, Sun Y. 2016. Clathrin-mediated endocytosis in budding yeast at a glance. *J Cell Sci* **129**:1531–1536. doi:10.1242/jcs.182303

Manenschijn HE, Picco A, Mund M, Ries J, Kaksonen M. 2019. Type-I myosins promote actin polymerization to drive membrane bending in endocytosis. *Elife* **17**:490011. doi:10.1101/490011

McIsaac RS, Silverman SJ, McClean MN, Gibney PA, Macinskas J, Hickman MJ, Petti AA, Botstein D. 2011. Fast-acting and nearly gratuitous induction of gene expression and protein depletion in *Saccharomyces cerevisiae*. *Mol Biol Cell* **22**:4447–4459. doi:10.1091/mbc.E11-05-0466

Mettlen M, Loerke D, Yarar D, Danuser G, Schmid SL. 2010. Cargo- and adaptor-specific mechanisms regulate clathrin-mediated endocytosis. *J Cell Biol* **188**:919–933. doi:10.1083/jcb.200908078

Newpher TM, Smith RP, Lemmon V, Lemmon SK. 2005. In vivo dynamics of clathrin and its adaptor-dependent recruitment to the actin-based endocytic machinery in yeast. *Dev Cell* **9**:87–98. doi:10.1016/j.devcel.2005.04.014

Nishimura K, Fukagawa T, Takisawa H, Kakimoto T, Kanemaki M. 2009. An auxin-based degron system for the rapid depletion of proteins in nonplant cells. *Nat Methods* **6**:917–922. doi:10.1038/nmeth.1401

Pedersen RTA, Drubin DG. 2019. Type I myosins anchor actin assembly to the plasma membrane during clathrin-mediated endocytosis. *J Cell Biol* **218**:1138–1147. doi:10.1083/jcb.201810005

Peng Y, Grassart A, Lu R, Wong CCL, Yates J, Barnes G, Drubin DG. 2015a. Casein Kinase 1 Promotes Initiation of Clathrin-Mediated Endocytosis. *Dev Cell* **32**:231–240. doi:10.1016/j.devcel.2014.11.014

Peng Y, Moritz M, Han X, Giddings TH, Lyon A, Kollman J, Winey M, Yates III J, Agard DA, Drubin DG, Barnes G. 2015b. Interaction of CK1δ with TuSC ensures proper microtubule assembly and spindle positioning. *Mol Biol Cell* **26**:1–37. doi:10.1091/mbc.E14-12-1627

Picco A, Mund M, Ries J, Nedelec F, Kaksonen M. 2015. Visualizing the functional architecture of the endocytic machinery. *Elife* **4**:1–29. doi:10.7554/eLife.04535

Pringle JR, Preston RA, Adams AEM, Stearns T, Drubin DG, Haarer BK, Jones EW. 1989. Fluorescence Microscopy Methods for Yeast. *Methods Cell Biol* **31**:357–435. doi:10.1016/S0091-679X(08)61620-9

Puthenveedu MA, von Zastrow M. 2006. Cargo Regulates Clathrin-Coated Pit Dynamics. *Cell* **127**:113–124. doi:10.1016/j.cell.2006.08.035

Reed GF, Lynn F, Meade BD. 2002. Use of Coefficient of Variation in Assessing Variability of Quantitative Assays. *Clin Diagn Lab Immunol* **9**:1235–1239. doi:10.1128/CDLI.9.6.1235

Skruzny M, Brach T, Ciuffa R, Rybina S, Wachsmuth M, Kaksonen M. 2012. Molecular basis for coupling the plasma membrane to the actin cytoskeleton during clathrin-mediated endocytosis. *Proc Natl Acad Sci U S A* **109**:E2533–E2542. doi:10.1073/pnas.1207011109

Stimpson HEM, Toret CP, Cheng AT, Pauly BS, Drubin DG. 2009. Early-Arriving Syp1p and Ede1p Function in Endocytic Site Placement and Formation in Budding Yeast. *Mol Biol Cell* **20**:4640–4651. doi:10.1091/mbc.E09

Sun Y, Leong NT, Jiang T, Tangara A, Darzacq X, Drubin DG. 2017. Switch-like Arp2/3 activation upon WASP and WIP recruitment to an apparent threshold level by multivalent linker proteins in vivo. *Elife* **6**:1–25. doi:10.7554/elife.29140

Sun Y, Leong NT, Wong T, Drubin DG. 2015. A Pan1/End3/Sla1 complex links Arp2/3-mediated actin assembly to sites of clathrin-mediated endocytosis. *Mol Biol Cell* **26**:3841–3856. doi:10.1091/mbc.E15-04-0252

Sun Y, Martin AC, Drubin DG. 2006. Endocytic Internalization in Budding Yeast Requires Coordinated Actin Nucleation and Myosin Motor Activity. *Dev Cell* **11**:33–46. doi:10.1016/j.devcel.2006.05.008

Sun Y, Schoeneberg J, Chen S, Jiang T, Kaplan C, Xu K, Pollard TD, Drubin DG. 2019. Direct comparison of clathrin-mediated endocytosis in budding and fission yeast reveals conserved and evolvable features. *bioRxiv* 733543. doi:10.1101/733543

Takizawa PA, Derisi JL, Wilhelm JE, Vale RD. 2000. Plasma Membrane Compartmentalization in Yeast by Messenger RNA Transport and a Septin Diffusion Barrier. *Science* **290**:341–344. doi:10.1126/science.290.5490.341

Taylor MJ, Perrais D, Merrifield CJ. 2011. A high precision survey of the molecular dynamics of mammalian clathrin-mediated endocytosis. *PLoS Biol* **9**. doi:10.1371/journal.pbio.1000604

Tonikian R, Xin X, Toret CP, Gfeller D, Landgraf C, Panni S, Paoluzi S, Castagnoli L, Currell B, Seshagiri S, Yu H, Winsor B, Vidal M, Gerstein MB, Bader GD, Volkmer R, Cesareni G, Drubin DG, Kim PM, Sidhu SS, Boone C. 2009. Bayesian modeling of the yeast SH3 domain interactome predicts spatiotemporal dynamics of endocytosis proteins. *PLoS Biol* **7**. doi:10.1371/journal.pbio.1000218

Weinberg JS, Drubin DG. 2014. Regulation of Clathrin-mediated endocytosis by dynamic ubiquitination and deubiquitination. *Curr Biol* **24**:951–959. doi:10.1016/j.cub.2014.03.038

Figure 1: Quantitatively probing the budding yeast clathrin-mediated endocytosis pathway through systematic imaging

(A) Illustration of key steps in the budding yeast CME pathway. Mechanisms of site initiation, transition from the early, variable lifetime stages to the later, more regular lifetime stages, and initiation of actin assembly remain poorly understood. Diagram adapted from Tonikian et al., 2009. (B) Top: montage of Las17-GFP and Abp1-RFP recruitment to an endocytic site viewed *en face* by live two-color TIRF microscopy of budding yeast. Bottom: centroid position tracks in the x and y dimensions for the Las17-GFP (green) and Abp1-RFP (magenta) spots depicted in the montage. • - beginning, x – end. See Video 1. (C) Fluorescence intensity vs. time for Las17-GFP and Abp1-RFP spots depicted in panel B. Timepoints of note and key measurements recorded are indicated by dotted lines and arrows, respectively. (D – F) Box and whisker plots of the time from the appearance of the indicated GFP-tagged query protein to the appearance of (D) Ede1-RFP, (E) Sla1-mCherry, and (F) Abp1-RFP. Red lines are median values, boxes indicate interquartile range, and whiskers indicate full range of the data.

Figure 1 – Figure Supplement 1: Lifetimes and relative fluorescence intensities of GFP-tagged query proteins agree with prior results but reveal inherent variability

(A) Box and whisker plots of lifetimes of the indicated GFP-tagged query protein when colocalized with Ede1-RFP (left), Sla1-mCherry (center), and Abp1-RFP (right). (B) Box and whisker plots of maximum fluorescence intensity of the indicated GFP-tagged query protein imaged with reference to Ede1-RFP (left), Sla1-mCherry (center), and Abp1-RFP

(right). Red lines are median values, boxes indicate interquartile range, and whiskers indicate full range of the data.

Figure 2: Lifetime and maximum intensity are positively correlated for individual later arriving CME proteins, but are less correlated for earlier arriving proteins

(A – C) Scatterplots of maximum intensity vs. lifetime for (A) Ede1-GFP, (B) Las17-GFP, and (C) Sac6-GFP. Color indicates the normalized data density in the neighborhood around each point. Red lines are linear fits to the data with the indicated R^2 values. (D) Summary of linear fits to plots of maximum intensity vs. lifetime for the indicated GFP-tagged query proteins. The bar height and color indicate the normalized slope and the R^2 of the fit, respectively. The grayed area highlights proteins displaying similar behavior. Association of query protein signal with signal of the reference protein Abp1-RFP was used to eliminate spurious events. See Figure 2 Supplement 1 for all related scatter plots.

Figure 2 – Figure Supplement 1: Maximum intensity vs. lifetime plots for GFP-tagged query proteins

Scatter plots of query protein maximum intensity vs. lifetime for GFP-tagged (A) Ede1, (B) Syp1, (C) Sla2, (D) Pan1, (E) Las17, (F) Sla1, (G) Vrp1, (H) Bzz1, (I) Arc15, (J) Myo5, (K) Sac6, (L) Ark1, and (M) Rvs167. Color indicates the normalized data density in the neighborhood around each point. Red lines are linear fits to the data with the indicated R^2 value. Association of query protein signal with signal of the reference protein Abp1-RFP was used to eliminate spurious events.

Figure 3: Correlations between reference protein abundance and query protein lifetime provide further evidence for a regulatory transition point

(A – C) Scatterplots of the maximum intensities of Abp1-RFP vs. the lifetimes of (A) Ede1-GFP, (B) Las17-GFP, and (C) Sac6-GFP. Colors indicate the normalized data density in the neighborhood around each point. Red lines are linear fits to the data with the indicated R^2 value. (D) Summary of linear fits to plots of maximum Abp1-RFP intensity vs. lifetime for the indicated GFP-tagged query proteins. The bar height and color indicate the normalized slope and the R^2 of the fit, respectively. The grayed area highlights proteins displaying similar behavior. See Figure 3 Supplement 1 for all related scatter plots.

Figure 3 – Figure Supplement 1: Abp1-RFP maximum intensity vs. query protein lifetime plots for GFP-tagged query proteins

Scatter plots of Abp1-RFP maximum intensity vs. lifetime for GFP-tagged (A) Ede1, (B) Syp1, (C) Sla2, (D) Pan1, (E) Las17, (F) Sla1, (G) Vrp1, (H) Bzz1, (I) Arc15, (J) Myo5, (K) Sac6, (L) Ark1, and (M) Rvs167. Color indicates the normalized data density in the neighborhood around each point. Red lines are linear fits to the data with the indicated R^2 value.

Figure 4: CME protein lifetimes are correlated amongst earlier arriving proteins, but early protein lifetimes are not correlated with late protein lifetimes

(A – C) Scatterplots of the lifetimes of Abp1-RFP vs. the lifetimes of (A) Ede1-GFP, (B) Las17-GFP, and (C) Sac6-GFP. Colors indicate the normalized data density in the neighborhood around each point. Red lines are linear fits to the data with the indicated R^2

value. (D – F) Summaries of linear fits to plots of (D) Ede1-RFP, (E) Sla1-mCherry, and (F) Abp1-RFP lifetime vs. lifetime for the indicated GFP-tagged query proteins. The bar height and color indicate the normalized slope and the R^2 of the fit, respectively. See Figure Supplements 1 - 3 for all related scatter plots.

Figure 4 – Figure Supplement 1: Ede1-RFP lifetime vs. query protein lifetime plots for GFP-tagged query proteins.

Scatter plots of Ede1-RFP lifetime vs. query protein lifetime for GFP-tagged (A) Syp1, (B) Hrr25 (3X-GFP tagged), (C) Pal1, and (D) Apl1. Color indicates the normalized data density in the neighborhood around each point. Red lines are linear fits to the data with the indicated R^2 value.

Figure 4 – Figure Supplement 2: Sla1-mCherry lifetime vs. query protein lifetime plots for GFP-tagged query proteins.

Scatter plots of Sla1-mCherry lifetime vs. query protein lifetime for GFP-tagged (A) Ede1, (B) Syp1, (C) Hrr25 (3X-GFP tagged), (D) Pal1, and (E) Apl1. Color indicates the normalized data density in the neighborhood around each point. Red lines are linear fits to the data with the indicated R^2 value.

Figure 4 – Figure Supplement 3: Abp1-RFP lifetime vs. query protein lifetime plots for GFP-tagged query proteins.

Scatter plots of Abp1-RFP lifetime vs. query protein lifetime for GFP-tagged (A) Ede1, (B) Syp1, (C) Sla2, (D) Pan1, (E) Las17, (F) Sla1, (G) Vrp1, (H) Bzz1, (I) Arc15, (J) Myo5, (K)

Sac6, (L) Ark1, and (M) Rvs167. Color indicates the normalized data density in the neighborhood around each point. Red lines are linear fits to the data with the indicated R^2 value.

Figure 5: Proximity to sites of exocytosis and cell polarity signaling influences the rate of endocytic site maturation.

(A) Montage from a maximum intensity-projected epifluorescence video of a cell endogenously expressing Sla1-mCherry (magenta) and Ede1-GFP (Green). Times are hours:minutes. See Video 2. (B) Maximum intensity projections of z-stacks (left) of polarized and depolarized cells paired with circumferential kymographs around the mother cortex from medial focal plane videos of the same cells (right) endogenously expressing Sla1-mCherry (magenta) and Ede1-GFP (Green). See Video 3. (C) Quantification of the ratio of the number of Sla1-mCherry sites to Ede1-GFP sites in mother cells from maximum intensity projections of z-stacks of 60 polarized and 60 depolarized cells. A two-tailed p value from a Mann-Whitney U test with the null hypothesis that the two ratios are identical (U = 1) is displayed. The median and interquartile ranges are denoted with error bars. (D) Percentage of 596 Ede1 patches from 59 polarized mother cells and 1034 Ede1 patches from 56 depolarized mother cells that persist throughout the duration of a 4-minute video (persistent), that are present at the start or end of the video (partial), or that assemble and disassemble within the interval of the video (turnover). Numbers indicate the percentage of patches observed in each category. A two-tailed p value from a Chi-Square test with the null hypothesis that the proportion distributions are identical (chi-square = 1349, 2 degrees of freedom) is displayed.

Figure 5 – Figure Supplement 1: Proximity to sites of exocytosis and cell polarity signaling does not influence the rate of late steps in the endocytic pathway

(A) Maximum intensity projections of z-stacks (top) of polarized and depolarized cells paired with radial kymographs of individual endocytic events from medial focal plane epifluorescence videos of the same cells (bottom) endogenously expressing Sla1-GFP (green) and Abp1-RFP (magenta). Kymograph generation and analysis were carried out in mother cells. (B) Quantification of the ratio of the number of Abp1-RFP sites to Sla1-GFP sites from maximum intensity projections of z-stacks of 50 polarized and 50 depolarized cells. Analysis was carried out in mother cells. A two-tailed p value from a Mann-Whitney U test with the null hypothesis that the two ratios are identical (U = 1051) is displayed. The median and interquartile ranges are denoted with error bars. (C) Sla1-GFP and Abp1-RFP lifetimes measured in mother cells of 40 polarized cells and 40 depolarized cells (5 representative sites per cell). Two-tailed p values from Mann-Whitney U tests (U_{Sla1} = 19732, U_{Abp1} = 17429) with the null hypothesis that the lifetimes are identical are displayed. The median and interquartile ranges are denoted with error bars.

Figure 6: Acute loss of cell polarity accelerates endocytic site maturation in small-budded mother cells.

(A) Maximum intensity projections of cells endogenously expressing polarity marker Bem1-GFP before and 5 minutes after 17-fold dilution into isotonic imaging media (control, left) or water (right). (B) Average ± standard deviation for Bem1-GFP intensity profiles

from 20 (media, left) and 30 (water, right) cells before and after dilution into the indicated media. Individual intensity profiles generated from 25 pixel-wide lines were normalized to the maximum value before dilution and to cell length. (C) Maximum intensity projections of a cell endogenously expressing Sla1-mCherry (magenta) and Ede1-GFP (green) before and 5 minutes after 17-fold dilution into water. (D) Quantification of the ratio of the number of Sla1-mCherry sites to Ede1-GFP sites from maximum intensity projections of z-stacks of 30 small-budded mother cells before and after osmotic shock. A two-tailed p value from a Mann-Whitney U test with the null hypothesis that the two ratios are identical (U = 7) is displayed. The median and interquartile ranges are denoted with error bars. (E) Circumferential kymographs around the mother cortex from medial focal plane videos of cells endogenously expressing Sla1-mCherry (magenta) and Ede1-GFP (Green) before and 5 minutes after 17-fold dilution into water. (F) Percentage of 280 Ede1 patches from 30 small-budded mother cells before and 594 Ede1 patches from 30 small-budded mother cells after osmotic shock that persist throughout the duration of a 4-minute video (persistent), are present at the start or end of the video (partial), or assemble and disassemble within the interval of the video (turnover). Numbers indicate the percentage of patches observed in each category. A two-tailed p value from a Chi-Square test with the null hypothesis that the proportions distributions are identical (chi-square = 543.1, 2 degrees of freedom) is displayed.

Figure 6, figure supplement 1: Acute loss of cell polarity does not accelerate late steps of the endocytic pathway

(A) Maximum intensity projections of cells endogenously expressing GFP-Sec4 before and 5 minutes after 17-fold dilution into isotonic imaging media (control, left) or water (right). (B) Maximum intensity projections of a cell endogenously expressing Sla1-GFP (Green) and Abp1-RFP (magenta) before and 5 minutes after 17-fold dilution into water. (C) Radial kymographs of individual endocytic events in small-budded mother cells from medial focal plane videos of cells endogenously expressing Sla1-GFP (green) and Abp1-RFP (magenta) before and 5 minutes after 17-fold dilution into water. (D) Quantification of the ratio of the number of Abp1-RFP sites to Sla1-GFP sites from maximum intensity projections of z-stacks of 30 small-budded mother cells before and after osmotic shock. A two-tailed p value from a Mann-Whitney U test with the null hypothesis that the two ratios are identical (U = 441.5) is displayed. The median and interquartile ranges are denoted with error bars. (E) Sla1-GFP and Abp1-RFP lifetimes measured in 30 small-budded mother cells prior to osmotic shock and 30 cells after osmotic shock (5 representative sites per cell). Two-tailed p values from Mann-Whiney U tests with the null hypothesis that the lifetimes are identical (U_{Sla1} = 1678, U_{Abp1} = 2998) are displayed. The median and interquartile ranges are denoted with error bars.

Figure 6, figure supplement 2: Testing whether Hrr25 regulates endocytic maturation

(A) Growth of cells of the indicated genotypes on YPD and auxin-containing plates at 18°C and 25°C. Photos are representative of results from three separate experiments. (B) Immunoblot illustrating degradation kinetics of auxin inducible degron (AID)-tagged Hrr25 upon treatment with auxin. Hrr25-AID was detected via a V5 epitope tag. Pgk1 was probed

as a loading control. (C) Quantification of relative Hrr25 levels as a function of treatment time in auxin from three independent experiments. Hrr25 band intensities were normalized to the Pgk1 loading control and expressed as a fraction of the preAuxin signal. (D) Percentage of Ede1 patches in 30 small-budded mother cells of the indicated genotype treated as indicated with auxin for 30 min. that persist throughout the duration of a 4-minute video (persistent), are present at the start or end of the video (partial), or assemble and disassemble within the interval of the video (turnover). Numbers indicate the percentage of patches observed in each category. Two-tailed p values from Chi-Square tests with the null hypothesis that the proportions distributions are identical are displayed. (E) Immunoblot illustrating overexpression of a 13myc-tagged copy of Hrr25 upon treatment with β-estradiol for 2 hours. Overexpressed Hrr25 was detected via the 13myc epitope tag. Endogenous Hrr25 and Pgk1 were probed directly as loading controls. (F) Percentage of Ede1 patches in 30 small-budded mother cells of the indicated genotype treated as indicated with β-estradiol for 2 hrs. analyzed as in panel D. Numbers indicate the percentage of patches observed in each category. Two-tailed p values from Chi-Square tests with the null hypothesis that the proportions distributions are identical are displayed.

Figure 7: Defining molecular components of the early and late steps of the endocytic pathway

(A) Maximum intensity projections of epifluorescence z-stacks of clusters of cells endogenously expressing Sla1-mCherry (magenta) and Syp1-GFP (green, first row), Sla2-GFP (green, second row), Ent2-GFP (green, third row), and Pan1-GFP (green, last row). Individual channels are shown in gray scale at left. (B) Quantification of the ratio of the

number of Sla1-mCherry sites to the number of Syp1-GFP (top row), Sla2-GFP (second row), Ent2-GFP (third row), and Pan1-GFP (last row) sites from maximum intensity projections of z-stacks of 30 small-budded mother cells before and after osmotic shock. Two-tailed p values from Mann-Whitney U test with the null hypothesis that the two ratios are identical are displayed ($U_{Syp1} = 0$, $U_{Sla2} = 0$, $U_{Ent2} = 0$, $U_{Pan1} = 448$). The median and interquartile ranges are denoted with error bars.

Figure 7, figure supplement 1: Defining molecular components of the early and late steps of the endocytic pathway

Maximum intensity projections of spinning disc confocal z-stacks of clusters of cells endogenously expressing Sla1-mCherry (magenta) and Hrr25-3xGFP (green, top), Apl1-GFP (green, second row), Pal1-GFP (green, third row), or Ent1-GFP (green, last row). Individual channels are shown in gray scale at left. Images are representative of at least three separate experiments

Figure 8: Cargo regulates the transition between two quantitatively distinguishable phases of endocytosis.

(A) Revised timeline for the clathrin-mediated endocytosis pathway indicating the proposed temporal location of the cargo checkpoint. Proteins upstream and downstream of the checkpoint are listed under each respective phase. (B) Schematic cartoon illustrating the proposed mechanism leading to polarized endocytosis in budding yeast. In highly polarized cells, endocytic cargos (black arrows) are delivered primarily to the growing bud by exocytosis (gray arrows), locally accelerating the transition from the initiation and

cargo-collection phase of CME (green spots) into the internalization phase (magenta spots). As exocytosis becomes depolarized later in the cell cycle, cargos are more plentiful across the plasma membrane, leading to global acceleration of maturation through the cargo checkpoint.

Video 1: Related to Figure 1B

TIRFM movie of several yeast cells endogenously expressing Las17-GFP (green) and Abp1-RFP (magenta). Each Las17 punctum is punctuated by a burst of Abp1 signal. Frames are separated by 1 second and played back at 15 frames per second (fps).

Video 2: Related to Figure 5A

Time-lapse of maximum intensity projections from epifliorescence z-stacks of a cell endogenously expressing Sla1-mCherry (magenta) and Ede1-GFP (green). A dynamic cycle of polarization/depolarization is apparent for the magenta Sla1 sites, but less apparent for the green Ede1 sites. Frames are separated by 10 minutes and played back at 10 fps.

Video 3: Related to Figure 5B

Epifluorescence movies in the media focal plane of the polarized and depolarized cells displayed in Figure 5B. The cells endogenously express Sla1-mCherry (magenta) and Ede1-GFP (green). Persistent Ede1 sites are present in the mother of the polarized cell (left), but not in the mother of the depolarized cell (right). Frames are separated by 2 seconds and played back at 15 fps. Circumferential kymographs in Figure 5B were generated from these movies.

Figure 1

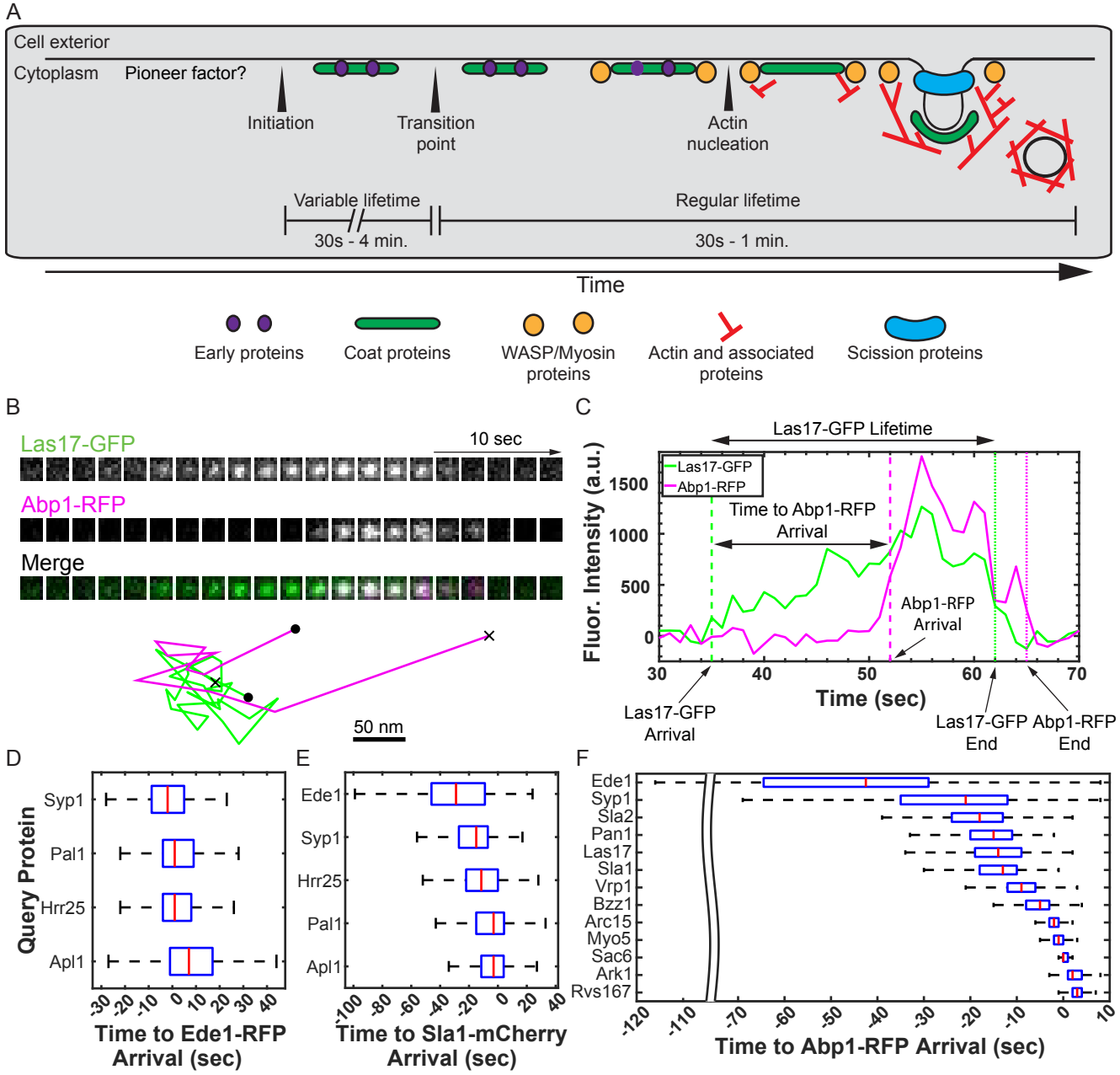
A
Cell exterior
Cytoplasm
Pioneer factor?
Initiation
Transition point
Actin nucleation
Variable lifetime
30s - 4 min.
Regular lifetime
30s - 1 min.
Time
Early proteins
Coat proteins
WASP/Myosin proteins
Actin and associated proteins
Scission proteins
B
Las17-GFP
10 sec
Abp1-RFP
Merge
50 nm
C
Las17-GFP Lifetime
Las17-GFP
Abp1-RFP
Time to Abp1-RFP Arrival
Abp1-RFP Arrival
Fluor. Intensity (a.u.)
Time (sec)
Las17-GFP Arrival
Las17-GFP End
Abp1-RFP End
D
Query Protein
Syp1
Pal1
Hrr25
Apl1
Time to Ede1-RFP Arrival (sec)
E
Ede1
Syp1
Hrr25
Pal1
Apl1
Time to Sla1-mCherry Arrival (sec)
F
Ede1
Syp1
Sla2
Pan1
Las17
Sla1
Vrp1
Bzz1
Arc15
Myo5
Sac6
Ark1
Rvs167
Time to Abp1-RFP Arrival (sec)

Figure 1 - Figure Supplement 1

A

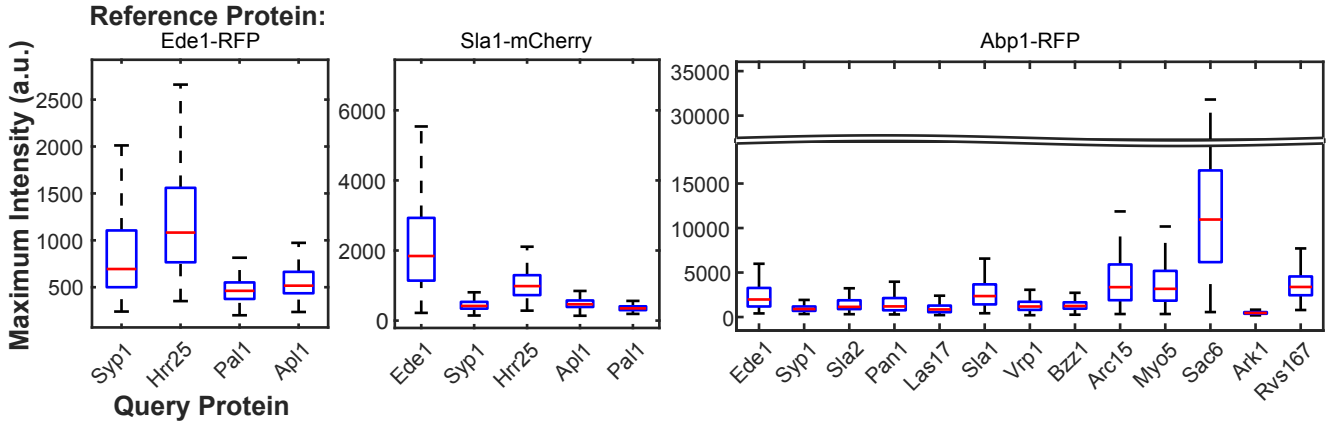

B

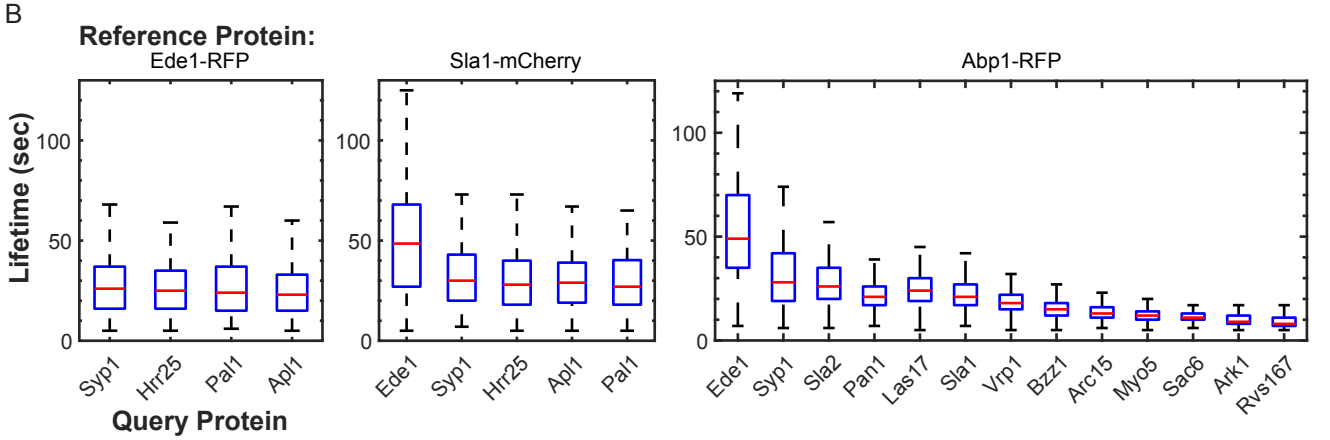

Figure 2

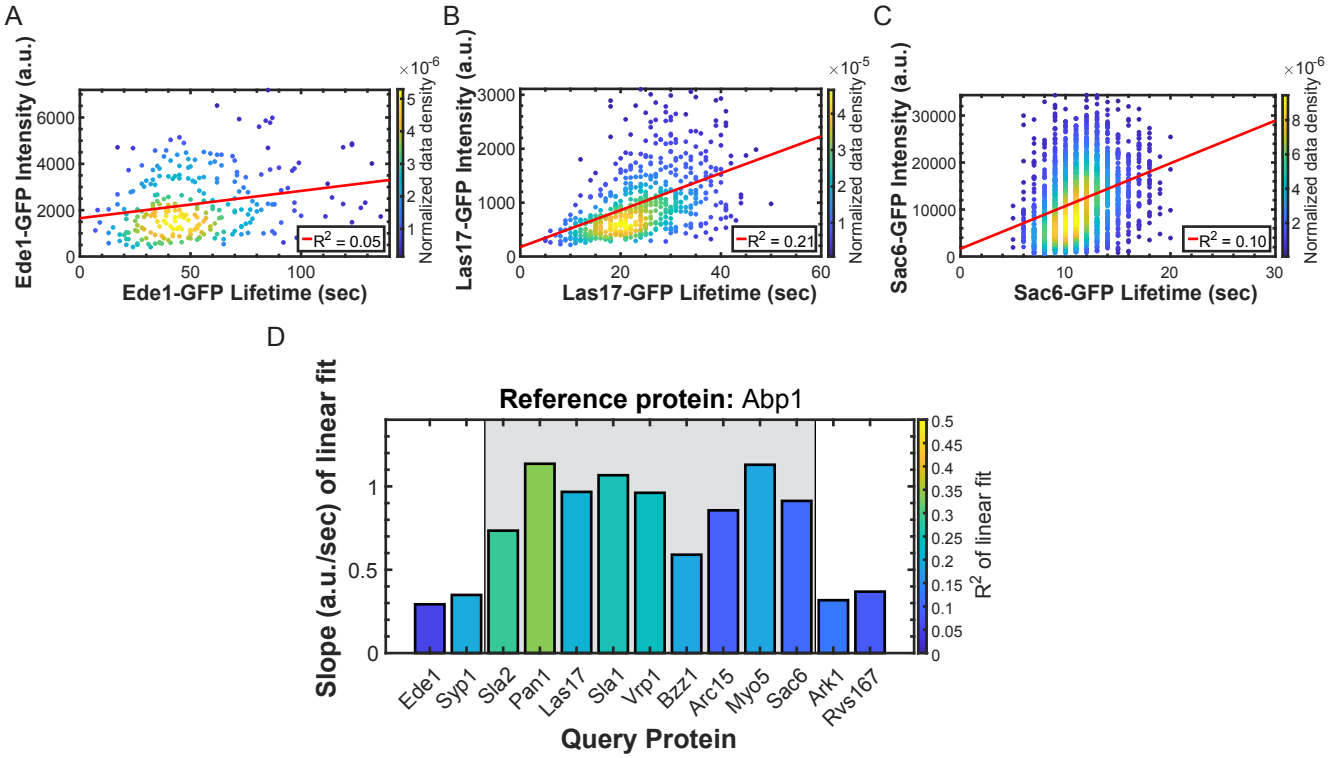
A
Ede1-GFP Intensity (a.u.)
Ede1-GFP Lifetime (sec)
Normalized data density
$\times 10^{-6}$
R^2 = 0.05
B
Las17-GFP Intensity (a.u.)
Las17-GFP Lifetime (sec)
Normalized data density
$\times 10^{-5}$
R^2 = 0.21
C
Sac6-GFP Intensity (a.u.)
Sac6-GFP Lifetime (sec)
Normalized data density
$\times 10^{-6}$
R^2 = 0.10
D
Reference protein: Abp1
Slope (a.u./sec) of linear fit
R^2 of linear fit
Ede1
Syp1
Sla2
Pan1
Las17
Sla1
Vrp1
Bzz1
Arc15
Myo5
Sac6
Ark1
Rvs167
Query Protein

Figure 2 - Figure Supplement 1

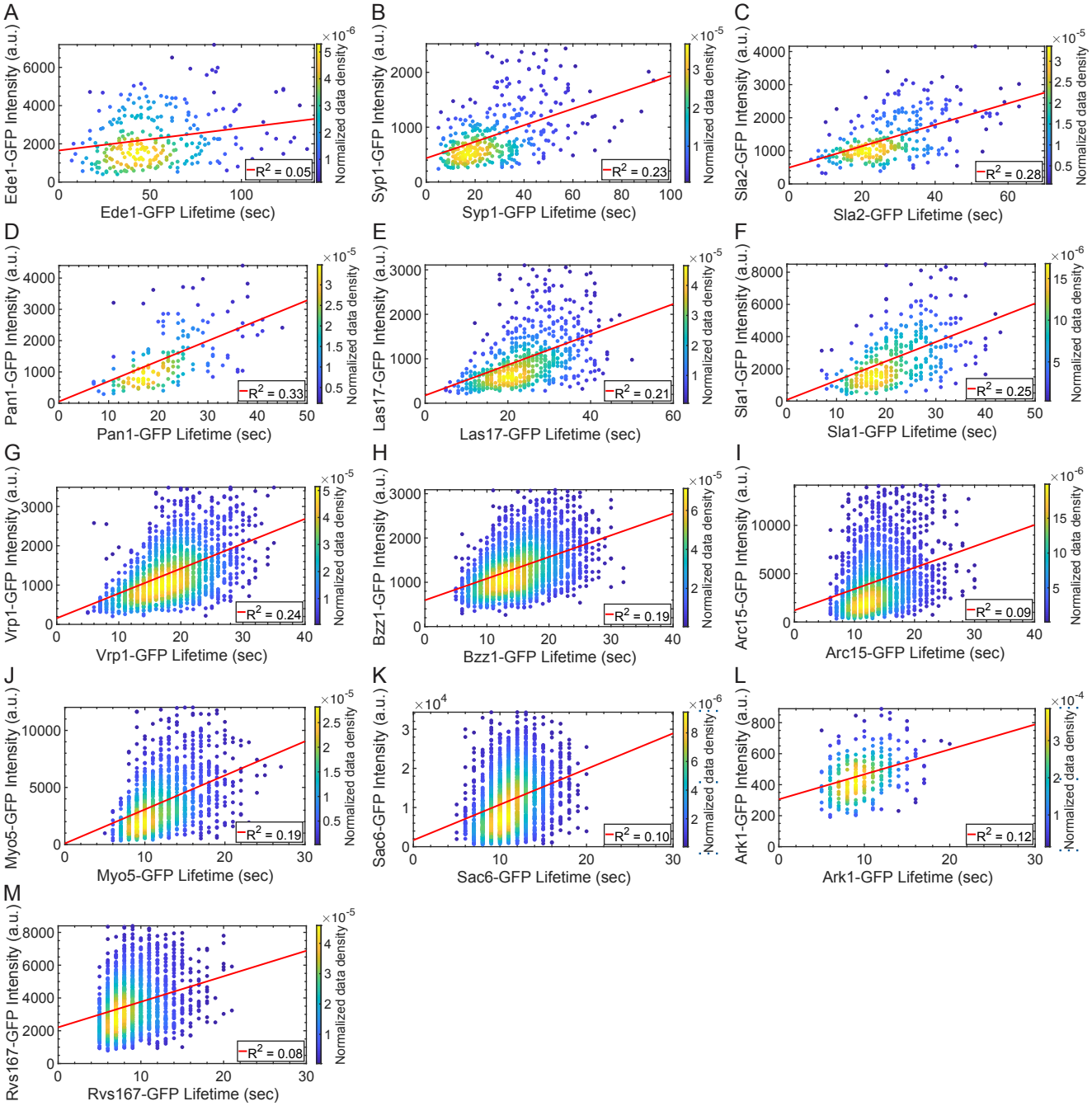

Figure 3

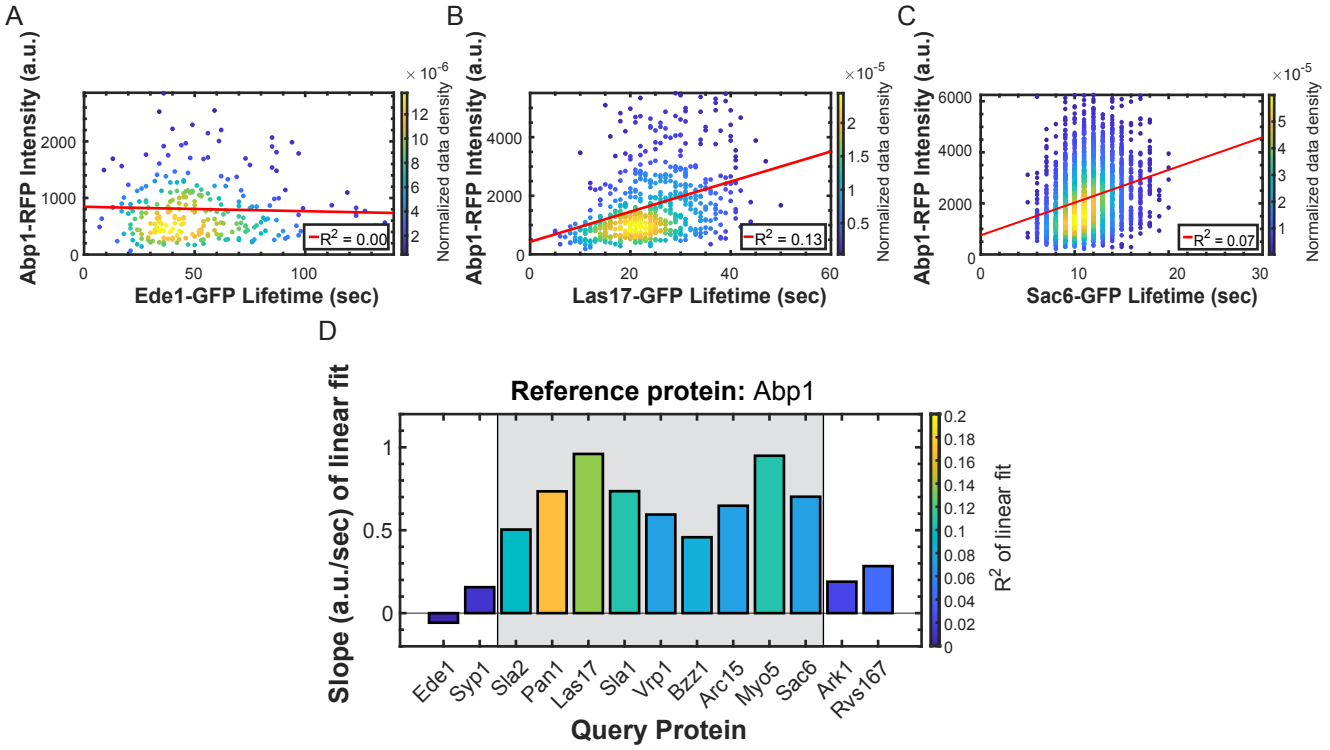
A
Abp1-RFP Intensity (a.u.)
Ede1-GFP Lifetime (sec)
R^2 = 0.00
Normalized data density
B
Abp1-RFP Intensity (a.u.)
Las17-GFP Lifetime (sec)
R^2 = 0.13
Normalized data density
C
Abp1-RFP Intensity (a.u.)
Sac6-GFP Lifetime (sec)
R^2 = 0.07
Normalized data density
D
Reference protein: Abp1
Slope (a.u./sec) of linear fit
R^2 of linear fit
Ede1
Syp1
Sla2
Pan1
Las17
Sla1
Vrp1
Bzz1
Arc15
Myo5
Sac6
Ark1
Rvs167
Query Protein

Figure 3 - Figure Supplement 1

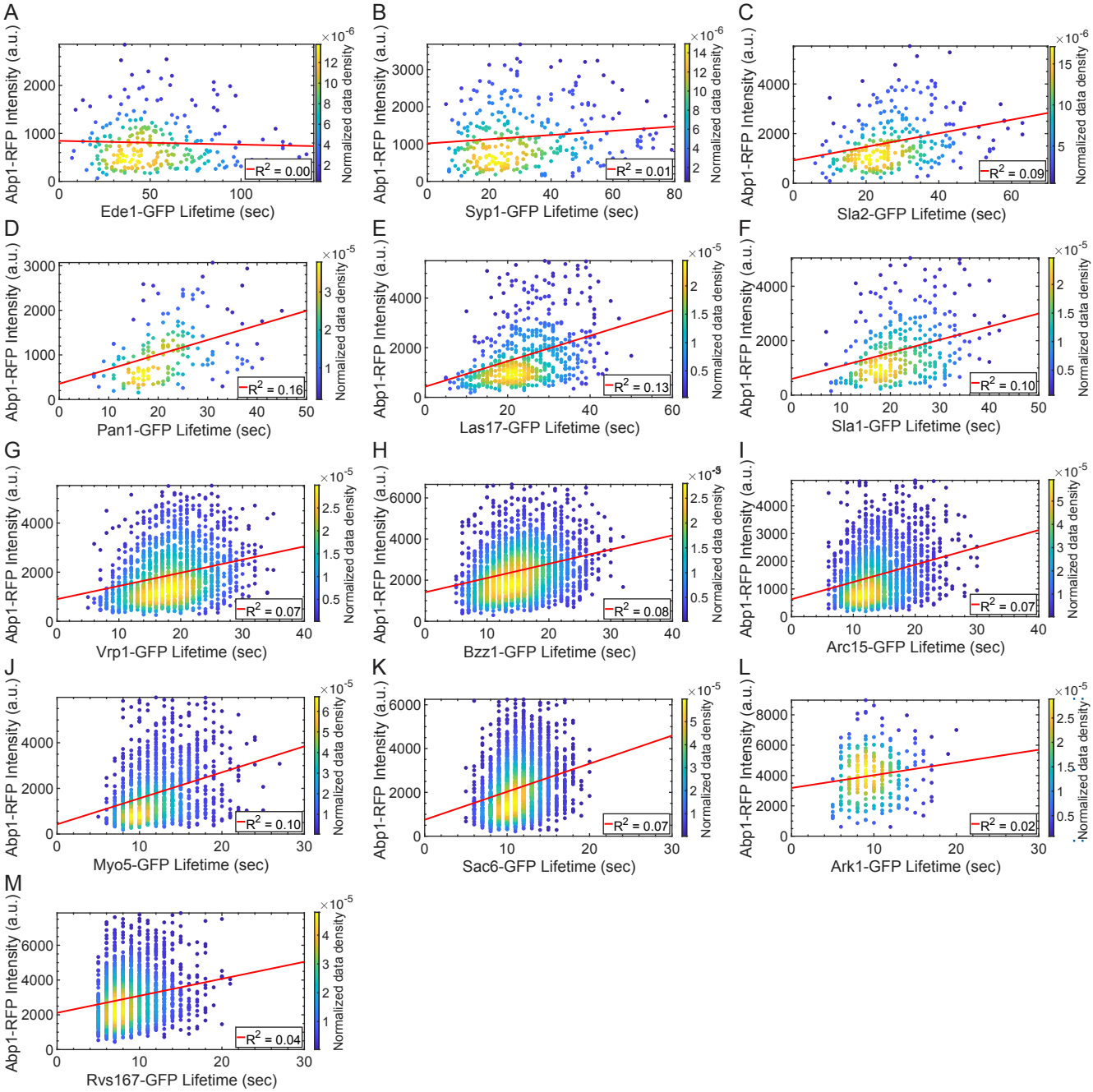

Figure 4

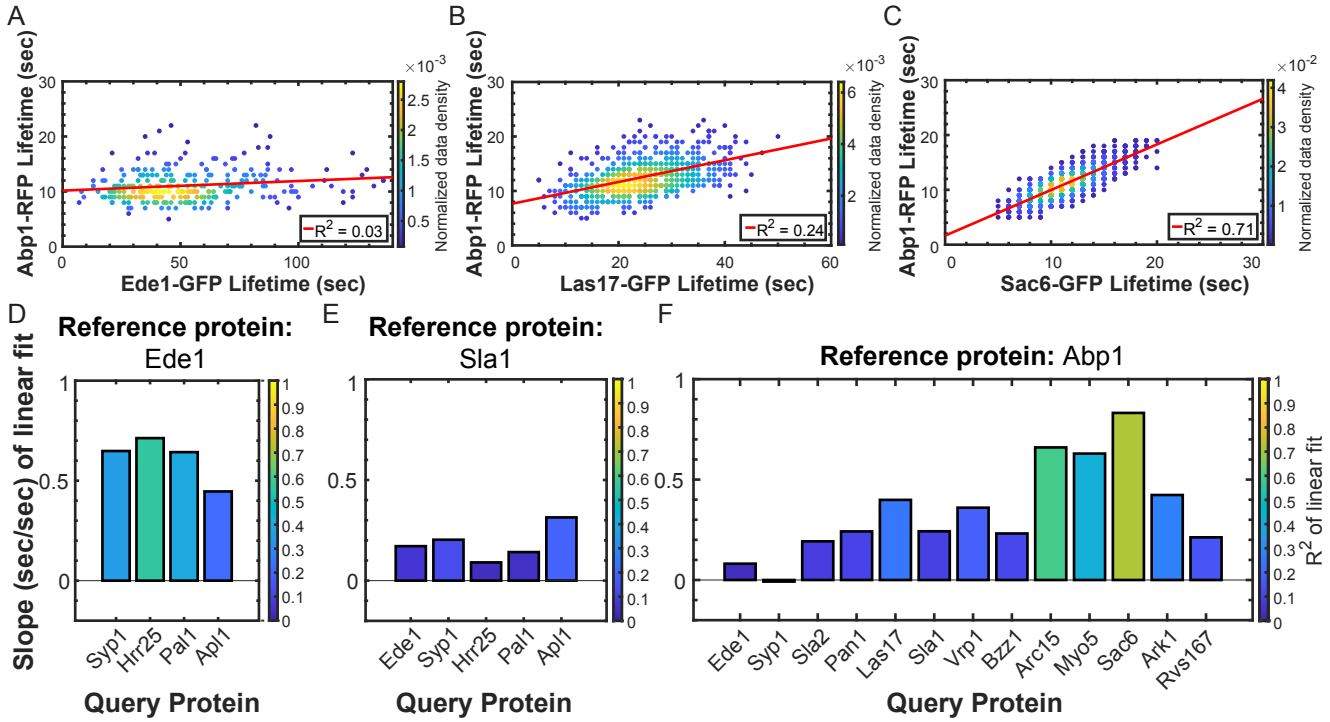
A
Abp1-RFP Lifetime (sec)
Ede1-GFP Lifetime (sec)
R2 = 0.03
Normalized data density
B
Las17-GFP Lifetime (sec)
R2 = 0.24
C
Sac6-GFP Lifetime (sec)
R2 = 0.71
D
Reference protein: Ede1
Slope (sec/sec) of linear fit
Syp1
Hrr25
Pal1
Apl1
Query Protein
E
Reference protein: Sla1
Ede1
Syp1
Hrr25
Pal1
Apl1
Query Protein
F
Reference protein: Abp1
Ede1
Syp1
Sla2
Pan1
Las17
Sla1
Vrp1
Bzz1
Arc15
Myo5
Sac6
Ark1
Rvs167
Query Protein
R2 of linear fit

Figure 4 - Figure Supplement 1

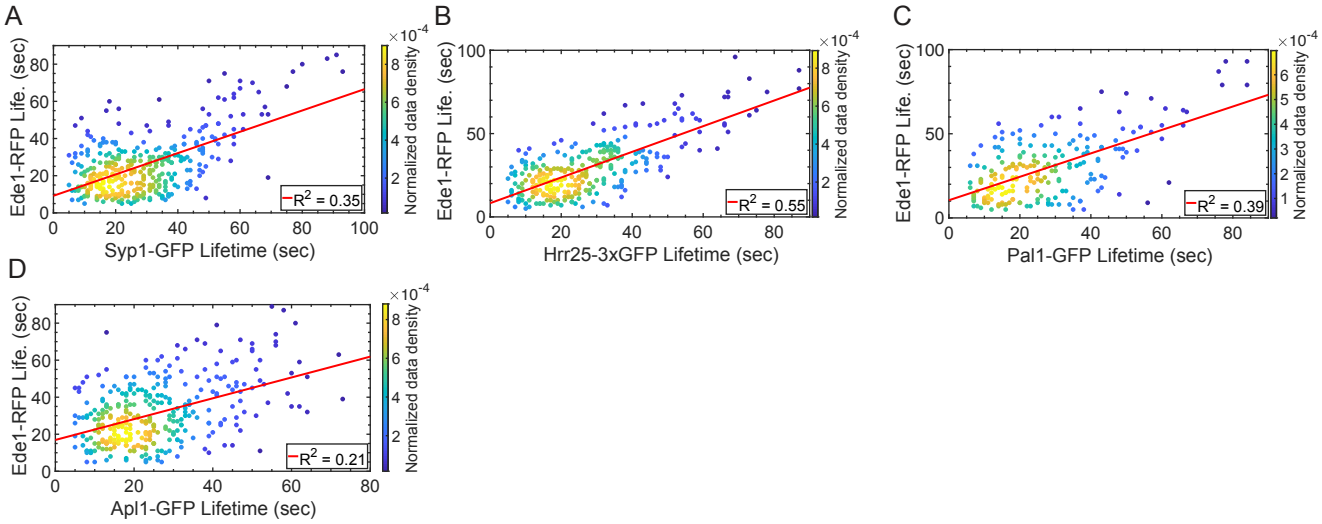

Figure 4 - Figure Supplement 2

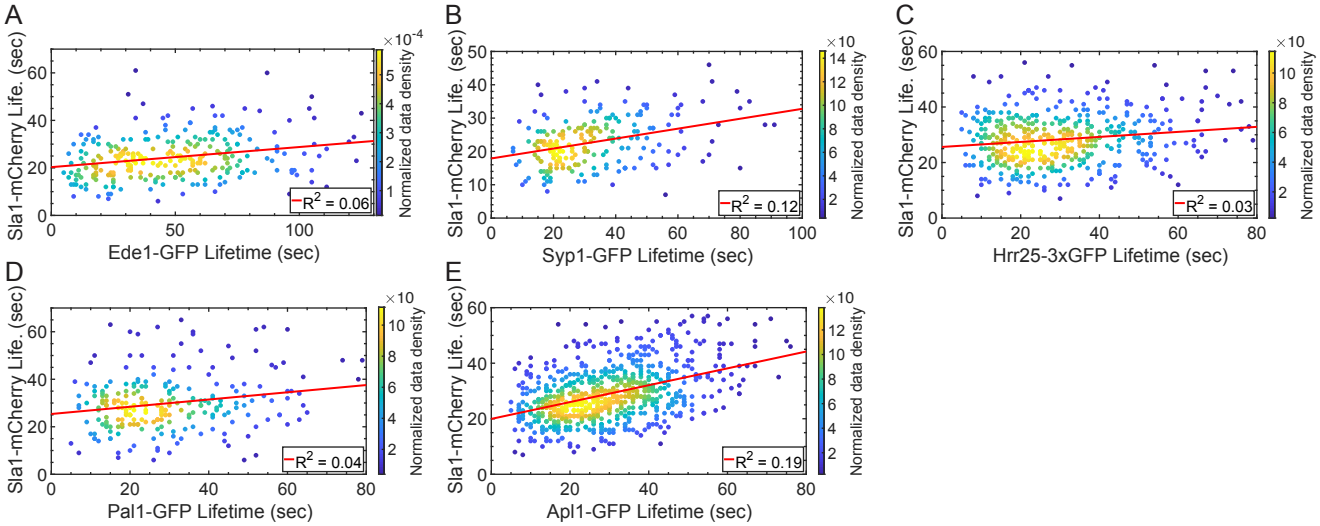

Figure 4 - Figure Supplement 3

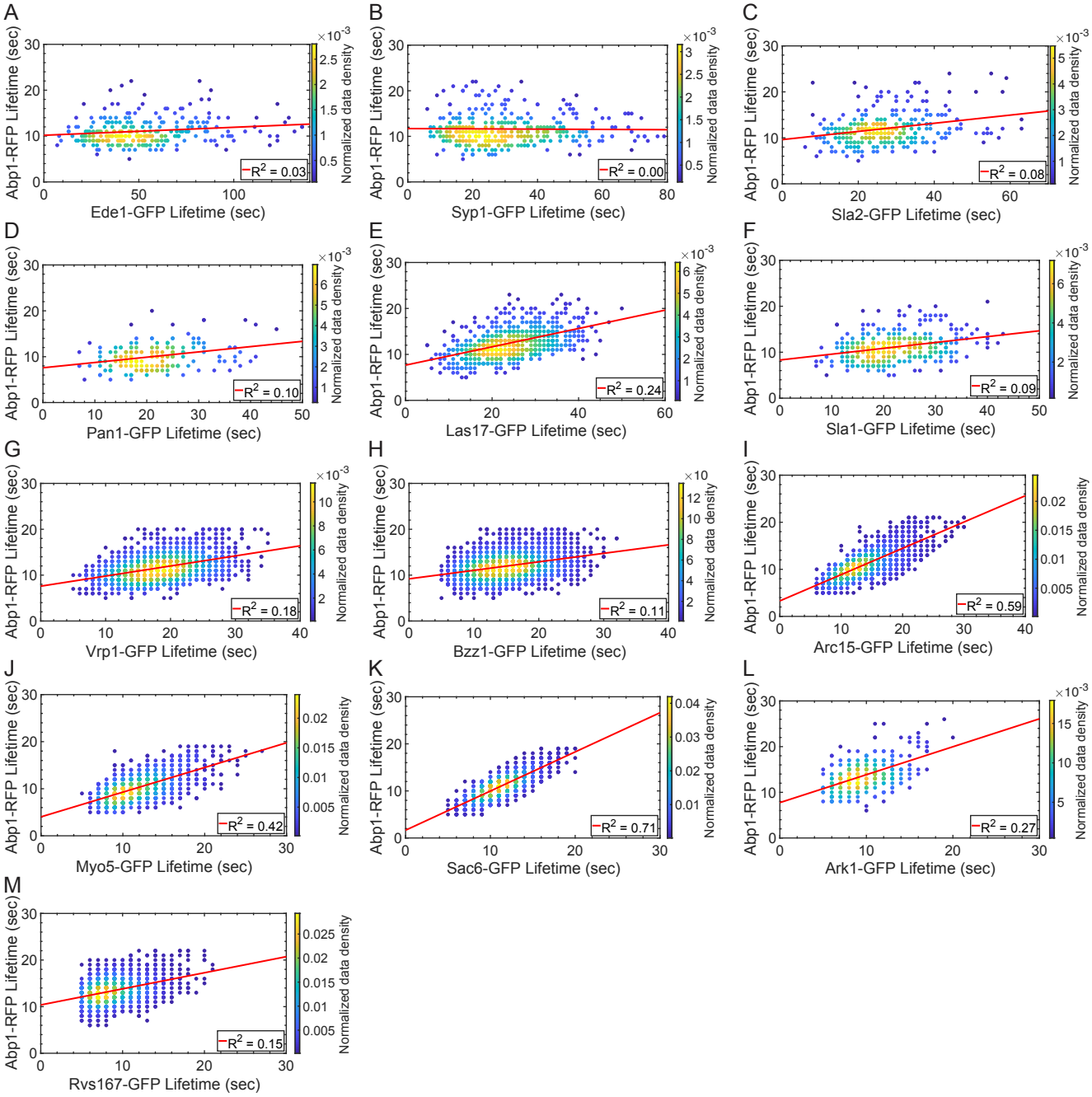

Figure 5

A

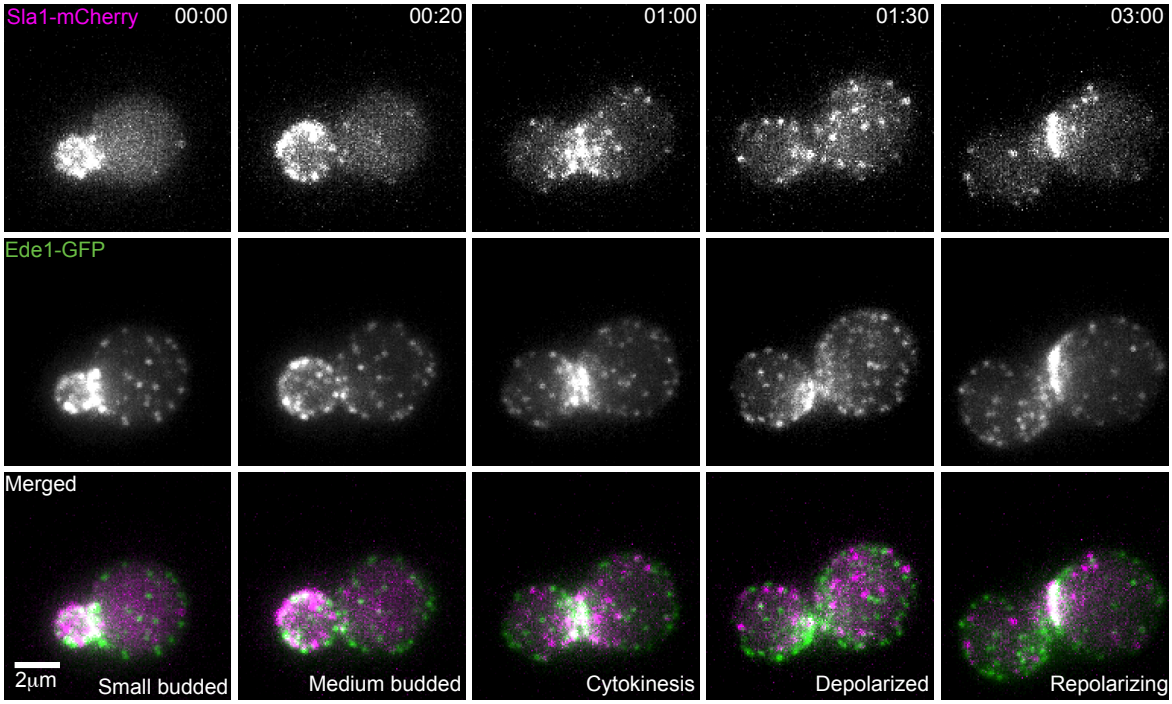

B

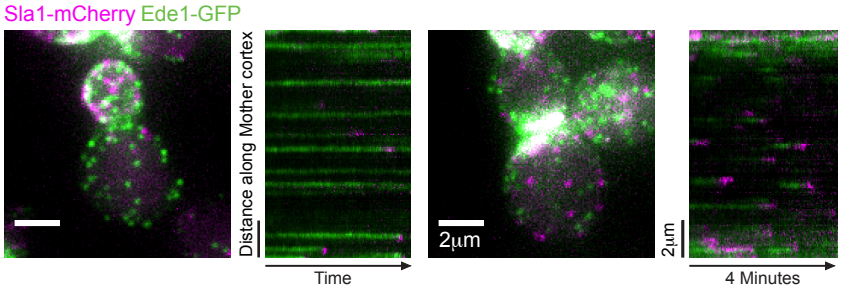

C

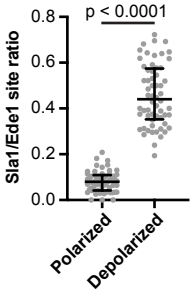

D

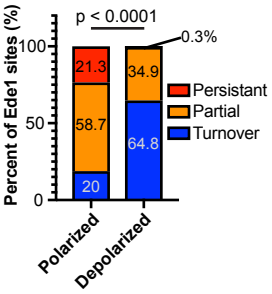

Figure 5 - Figure Supplement 1

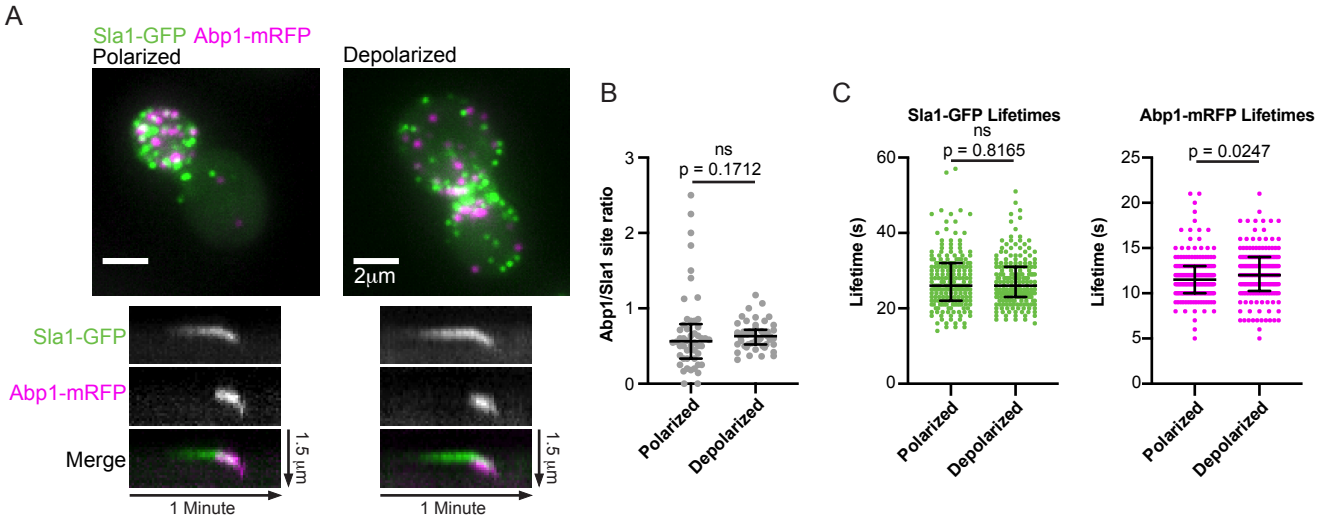

Figure 6

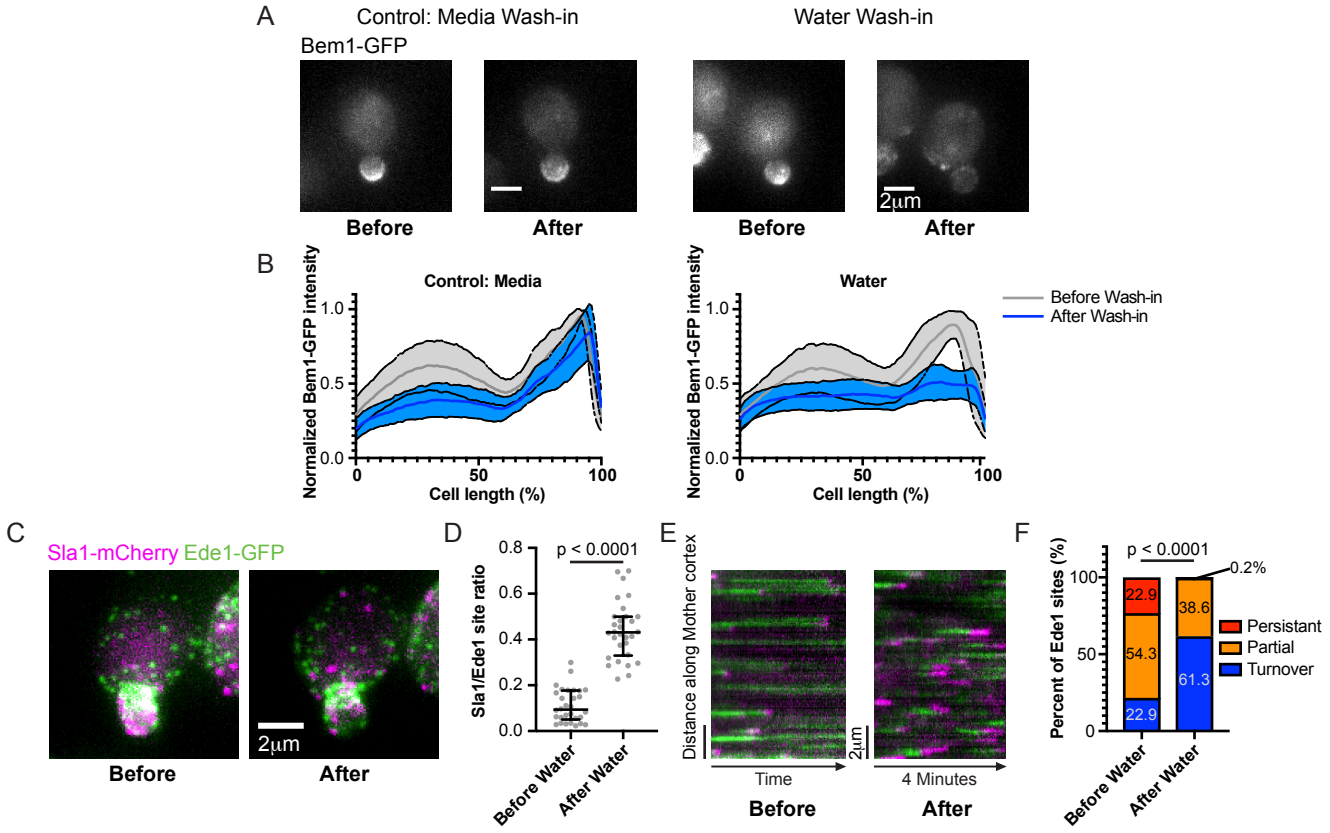
A
Control: Media Wash-in
Water Wash-in
Bem1-GFP
2µm
Before
After
Before
After
B
Control: Media
Water
Normalized Bem1-GFP intensity
Cell length (%)
Before Wash-in
After Wash-in
C
Sla1-mCherry Ede1-GFP
2µm
Before
After
D
p < 0.0001
Sla1/Ede1 site ratio
Before Water
After Water
E
Distance along Mother cortex
Time
2µm
4 Minutes
Before
After
F
p < 0.0001
0.2%
Percent of Ede1 sites (%)
22.9
54.3
22.9
38.6
61.3
Persistant
Partial
Turnover
Before Water
After Water

Figure 6 - Figure Supplement 1

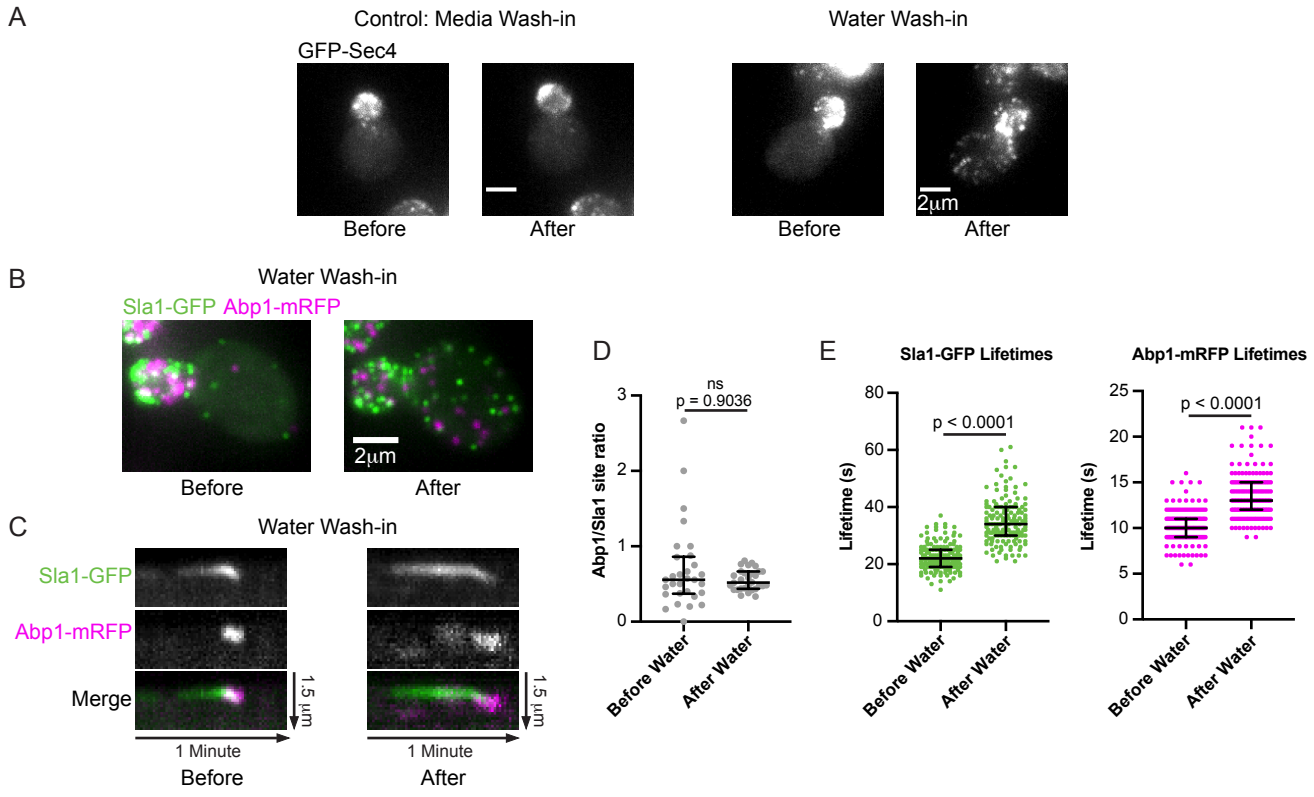

Figure 6 - Figure Supplement 2

A

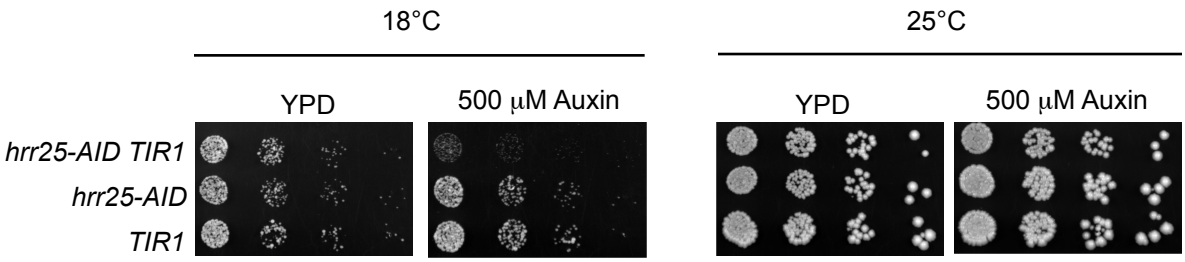

B

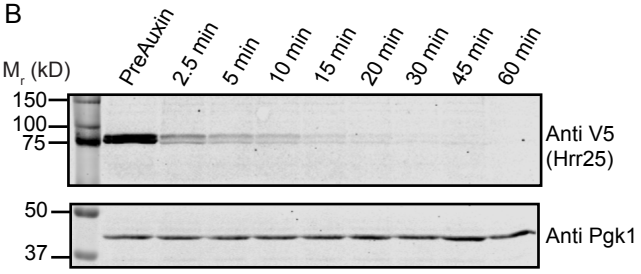

C

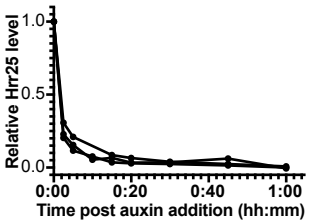

D

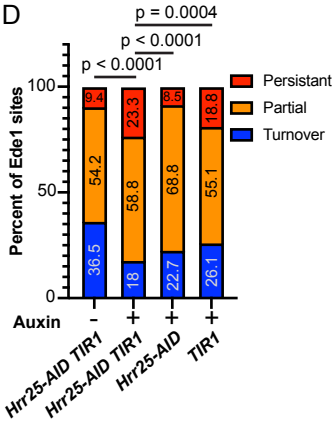

E

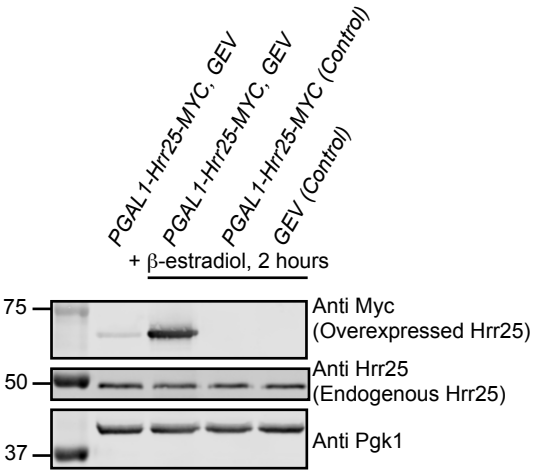

F

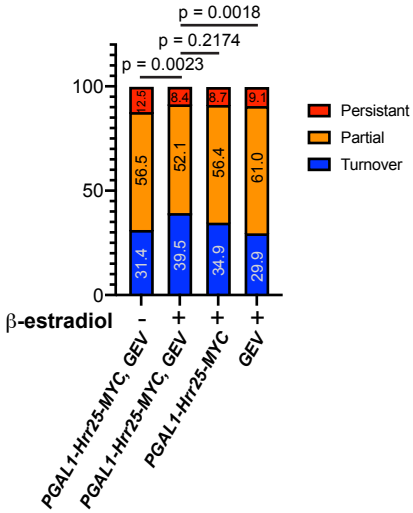

Figure 7

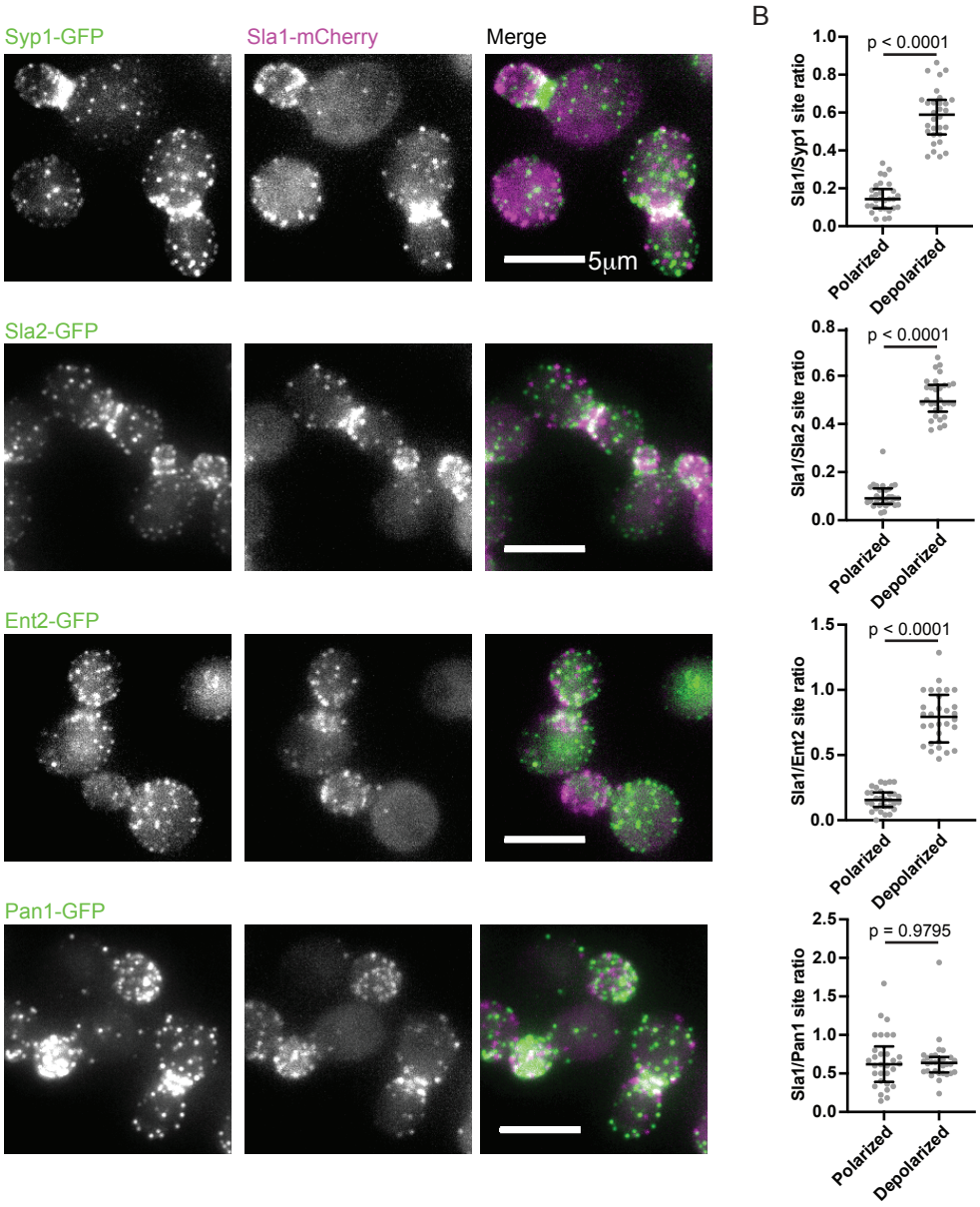
A
Syp1-GFP
Sla1-mCherry
Merge
5μm
Sla2-GFP
Ent2-GFP
Pan1-GFP
B
Sla1/Syp1 site ratio
p < 0.0001
Polarized
Depolarized
Sla1/Sla2 site ratio
p < 0.0001
Sla1/Ent2 site ratio
p < 0.0001
Sla1/Pan1 site ratio
p = 0.9795

Figure 7 - Figure Supplement 1

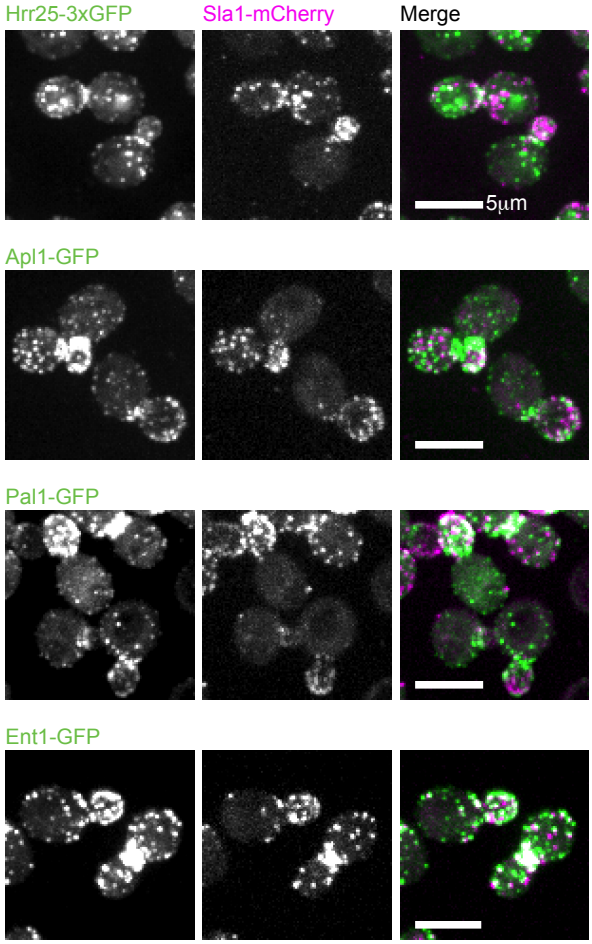

Figure 8

A

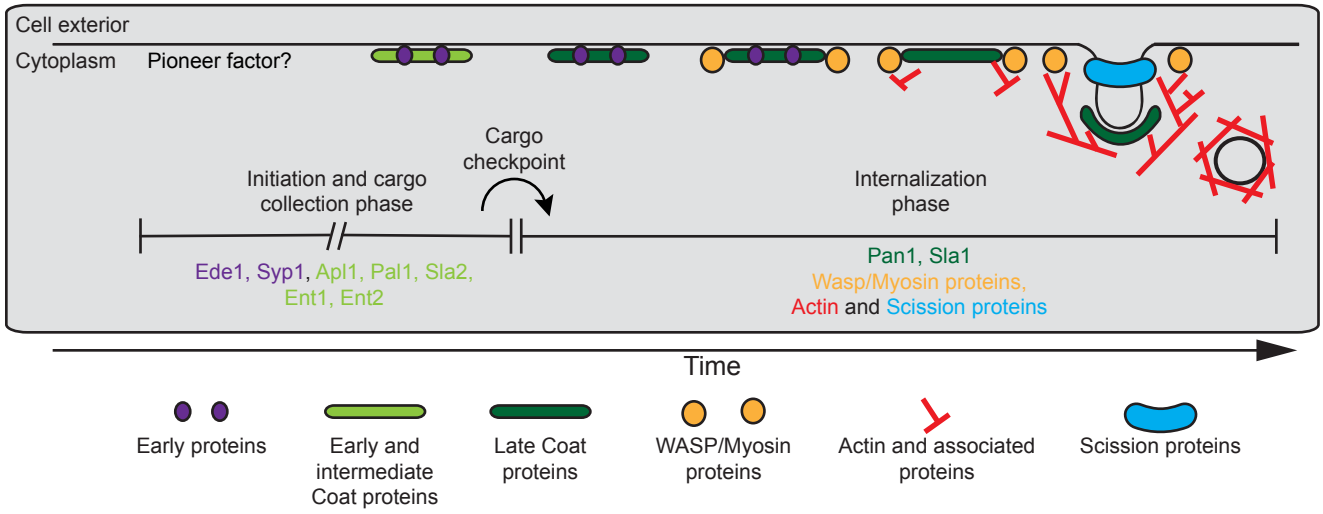
Cell exterior
Cytoplasm
Pioneer factor?
Cargo checkpoint
Initiation and cargo collection phase
Internalization phase
Ede1, Syp1, Apl1, Pal1, Sla2, Ent1, Ent2
Pan1, Sla1
Wasp/Myosin proteins,
Actin and Scission proteins
Time
Early proteins
Early and intermediate Coat proteins
Late Coat proteins
WASP/Myosin proteins
Actin and associated proteins
Scission proteins

B

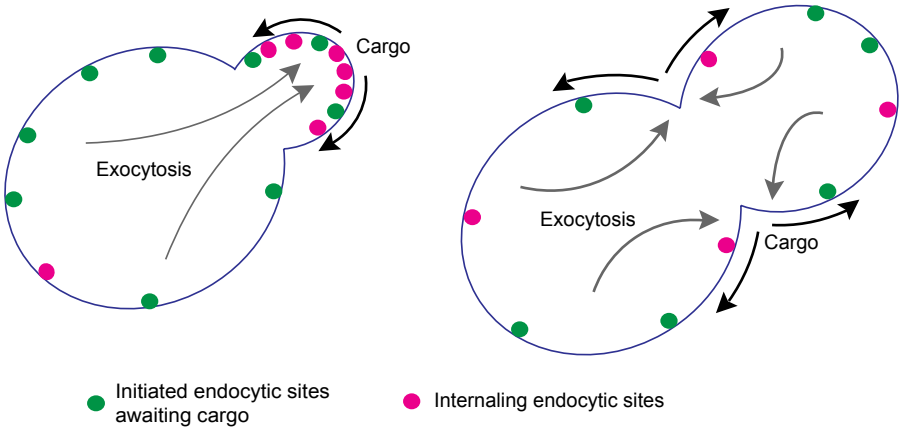
Cargo
Exocytosis
Exocytosis
Cargo
Initiated endocytic sites awaiting cargo
Internaling endocytic sites

Supplementary table 1: strains used in this study

Name	Genotype	Source
DDY1102	*MATa/MATα his3-Δ200/his3-Δ200, leu2-3, 112/leu2-3, 112, ura3-52/ura3-52, ade2-1/ADE2, lys2-801/LYS2*	Drubin Lab
DDY5713	*MATa his3-Δ200, leu2-3, 112, ura3-52, ABP1-mRFP::HIS3, SLA1-GFP::KanMX*	This study
DDY5714	*MATa his3-Δ200, leu2-3, 112, ura3-52, ABP1-mRFP::HIS3, Bzz1-GFP::HIS3*	This study
DDY5715	*MATa his3-Δ200, leu2-3, 112, ura3-52, ABP1-mRFP::HIS3, ARC15-GFP::KanMX*	This study
DDY5716	*MATa his3-Δ200, leu2-3, 112, ura3-52, ABP1-mRFP::HIS3, RVS167-GFP::HIS3*	This study
DDY5717	*MATa his3-Δ200, leu2-3, 112, ura3-52, ABP1-mRFP::HIS3, SLA2-GFP::HIS3*	This study
DDY5718	*MATa his3-Δ200, leu2-3, 112, ura3-52, ABP1-mRFP::HIS3, ARK1-GFP::KanMX*	This study
DDY5719	*MATa his3-Δ200, leu2-3, 112, ura3-52, ABP1-mRFP::HIS3, SAC6-GFP::HIS3*	This study
DDY5720	*MATa his3-Δ200, leu2-3, 112, ura3-52, bar1Δ::NatR, EDE1-mRFP::KanMX, PAL1-GFP::HIS3*	This study
DDY5721	*MATa his3-Δ200, leu2-3, 112, ura3-52, bar1Δ::NatR, EDE1-mRFP::HIS3, SYP1-GFP::KanMX*	This study
DDY5722	*MATa his3-Δ200, leu2-3, 112, ura3-52, bar1Δ::NatR, EDE1-mRFP::KanMX, Hrr25-3xGFP::HIS3*	This study
DDY5723	*MATa his3-Δ200, leu2-3, 112, ura3-52, bar1Δ::NatR, SLA1-mCherry::HIS3, PAL1-GFP::HIS3*	This study
DDY5724	*MATa his3-Δ200, leu2-3, 112, ura3-52, bar1Δ::NatR, SLA1-mCherry::HIS3, APL1-GFP::HIS3*	This study
DDY5725	*MATa his3-Δ200, leu2-3, 112, ura3-52, bar1Δ::NatR, SLA1-mCherry::HIS3, EDE1-GFP::HIS3*	This study
DDY5726	*MATa his3-Δ200, leu2-3, 112, ura3-52, bar1Δ::NatR, SLA1-mCherry::HIS3, SYP1-GFP::KanMX*	This study
DDY5727	*MATa his3-Δ200, leu2-3, 112, ura3-52, bar1Δ::NatR, SLA1-mCherry::HIS3, Hrr25-3xGFP::HIS3*	This study
DDY3293	*MATα his3-Δ200, leu2-3, 112, ura3-52, ABP1-mRFP::HIS3, LAS17-GFP::HIS3*	Drubin lab
DDY5617	*MATa his3-Δ200, leu2-3, 112, ura3-52, ABP1-mRFP::HIS3, LAS17-GFP::HIS3*	Drubin lab (Sun et al., 2017)
DDY3288	*MATa his3-Δ200, leu2-3, 112, ura3-52, ABP1-mRFP::HIS3, MYO5-GFP::URA3::KanMX*	Drubin lab
DDY5640	*MATa his3-Δ200, leu2-3, 112, ura3-52, ABP1-mRFP::HygMX, MYO5-GFP::HIS3*	Drubin lab (Sun et al., 2017)
DDY3063	*MATα his3-Δ200, leu2-3, 112, ura3-52, ABP1-mRFP::HIS3, Pan1-GFP::HIS3*	Drubin lab

DDY3314	*MATa his3-Δ200, leu2-3, 112, ura3-52, ABP1-mRFP::HIS3, Pan1-GFP::KanMX*	Drubin lab
DDY3867	*MATα his3-Δ200, leu2-3, 112, ura3-52, ABP1-mRFP::HIS3, SYP1-GFP::KanMX*	Drubin lab (Stimpson et al., 2009)
DDY3868	*MATa his3-Δ200, leu2-3, 112, ura3-52, ABP1-mRFP::HIS3, Ede1-GFP::HIS3*	Drubin lab (Stimpson et al., 2009)
DDY3061	*MATα his3-Δ200, leu2-3, 112, ura3-52, ABP1-mRFP::HIS3, CLC1-GFP::HIS3*	Drubin lab
DDY5635	*MATa his3-Δ200, leu2-3, 112, ura3-52, ABP1-mRFP::HygMX, VRP1-GFP::HIS3*	Drubin lab (Sun et al., 2017)
DDY3837	*MATα, his3-Δ200, leu2-3, 112, ura3-52, bar1Δ::LEU2, EDE1-mRFP::HIS3, APL1-GFP::HIS3*	Drubin lab
DDY5728	*MATα, his3Δ1, leu2Δ0, lys2Δ0, ura3Δ0, GFP-SEC4::URA3*	Bretscher lab (Donovan and Bretscher, 2015)
DDY4884	*MATα, his3-Δ200, leu2-3, 112, ura3-52, BEM1-GFP::HIS3*	Drubin Lab
DDY4083	*MATα, his3-Δ200, leu2-3, 112, ura3-52, SLA1-mCherry::HIS3, SLA2-GFP::HIS3*	Drubin lab (Carroll et al., 2012)
DDY4084	*MATα, his3-Δ200, leu2-3, 112, ura3-52, SLA1-mCherry::HIS3, ENT1-GFP::HIS3*	Drubin lab (Carroll et al., 2012)
DDY4085	*MATα, his3-Δ200, leu2-3, 112, ura3-52, SLA1-mCherry::HIS3, ENT2-GFP::HIS3*	Drubin lab (Carroll et al., 2012)
DDY4834	*MATα, his3-Δ200, leu2-3, 112, ura3-52, SLA1-mCherry::HIS3, PAN1-GFP::HIS3*	Drubin lab (Sun et al., 2015)

Supplementary table 2: Time to arrival for GFP-tagged query proteins colocalized with Ede1-RFP. Related to Figure 1D

Query protein	N	Median time to arrival (s)	Mean (s)	St. Dev (s)
Apl1	329	-7.0	-7.7	14.3
Hrr25	291	-1.0	-1.9	9.3
Pal1	207	-1.0	-2.6	12.0
Syp1	351	2.0	1.7	9.9

Supplementary table 3: Time to arrival for GFP-tagged query proteins colocalized with Sla1-mCherry. Related to Figure 1E

Query protein	N	Median time to arrival (s)	Mean (s)	St. Dev (s)
Apl1	728	3.0	3.8	12.1
Ede1	260	29.0	29.6	26.1
Hrr25	444	11.5	11.3	16.5
Pal1	229	3.0	6.0	15.7
Syp1	211	15.0	17.4	15.3

Supplementary table 4: Time to arrival for GFP-tagged query proteins colocalized with Abp1-RFP. Related to Figure 1F

Query protein	N	Median time to arrival (s)	Mean (s)	St. Dev (s)
Arc15	1878	2.0	2.3	2.5
Ark1	260	-2.0	-2.3	2.2
Bzz1	2257	5.0	5.7	3.9
Ede1	252	42.5	48.0	27.9
Las17	582	14.0	14.1	6.9
Myo5	1202	1.0	1.5	1.8
Pan1	158	15.0	16.3	6.7
Rvs167	1802	-3.0	-3.1	2.0
Sac6	2512	0.0	0.0	1.1
Sla1	316	13.0	14.0	5.9
Sla2	274	18.0	18.9	9.9
Syp1	315	21.0	24.3	17.6
Vrp1	1604	9.0	9.0	4.4

Supplementary table 5: Maximum fluorescence intensity of GFP-tagged query proteins colocalized with Ede1-RFP. Related to Figure 1, Figure supplement 1A

Query protein	N	Median maximum intensity (au)	Mean (au)	St. Dev (au)
Apl1	329	517	565	186
Hrr25	291	1083	1199	542
Pal1	207	462	483	160
Syp1	351	694	868	508

Supplementary table 6: Maximum fluorescence intensity of GFP-tagged query proteins colocalized with Sla1-mCherry. Related to Figure 1, Figure supplement 1A

Query protein	N	Median maximum intensity (au)	Mean (au)	St. Dev (au)
Apl1	728	466	486	140
Ede1	260	1843	2183	1434
Hrr25	444	984	1052	441
Pal1	229	349	363	97
Syp1	211	419	461	183

Supplementary table 7: Maximum fluorescence intensity of GFP-tagged query proteins colocalized with Abp1-RFP. Related to Figure 1, Figure supplement 1A

Query protein	N	Median maximum intensity (au)	Mean (au)	St. Dev (au)
Arc15	1878	3358	4291	3116
Ark1	260	457	465	142
Bzz1	2257	1241	1342	539
Ede1	252	1972	2292	1364
Las17	582	851	1012	615
Myo5	1202	3168	3743	2457
Pan1	158	1196	1479	896
Rvs167	1802	3378	3620	1558
Sac6	2512	10954	11916	7004
Sla1	316	2356	2749	1717
Sla2	274	1144	1399	687
Syp1	315	899	979	405
Vrp1	1604	1183	1329	681

Supplementary table 8: Lifetimes of GFP-tagged query proteins colocalized with Ede1-RFP. Related to Figure 1, Figure supplement 1B

Query protein	N	Median lifetime (s)	Mean lifetime (s)	St. Dev (s)	Coeff. of variation
Apl1	329	23.0	25.7	13.9	0.54
Hrr25	291	25.0	27.9	16.0	0.57
Pal1	207	24.0	27.6	16.5	0.60
Syp1	351	26.0	28.8	16.2	0.56

Supplementary table 9: Lifetimes of GFP-tagged query proteins colocalized with Sla1-mCherry. Related to Figure 1, Figure supplement 1B

Query protein	N	Median lifetime (s)	Mean lifetime (s)	St. Dev (s)	Coeff. of variation
Apl1	728	29.0	30.0	13.7	0.46
Ede1	260	48.5	49.5	27.4	0.55
Hrr25	444	28.0	30.5	15.8	0.52
Pal1	229	27.0	29.9	15.5	0.52
Syp1	211	30.0	33.3	17.2	0.52

Supplementary table 10: Lifetimes of GFP-tagged query proteins colocalized with Sla1-mCherry. Related to Figure 1, Figure supplement 1B

Query protein	N	Median lifetime (s)	Mean lifetime (s)	St. Dev (s)	Coeff. of variation
Arc15	1878	13.0	14.0	4.2	0.3
Ark1	260	9.0	9.9	3.0	0.3
Bzz1	2257	15.0	15.3	4.8	0.32
Ede1	252	49.0	54.2	26.7	0.49
Las17	582	24.0	24.4	8.3	0.34
Myo5	1202	12.0	12.3	3.6	0.29
Pan1	158	21.0	22.0	7.9	0.36
Rvs167	1802	8.0	9.1	2.9	0.32
Sac6	2512	11.0	11.3	2.5	0.22
Sla1	316	21.0	22.3	7.2	0.32
Sla2	274	26.0	28.0	11.2	0.40
Syp1	315	28.0	31.6	16.2	0.51
Vrp1	1604	18.0	18.6	5.3	0.29

Supplementary table 11: Fit statistics from linear fits of intensity vs. lifetime plots for GFP-tagged query proteins. Upper and lower bounds indicate the 95% confidence interval. Related to Figure 2D

Query protein	N	Slope	Slope upper bound	Slope lower bound	R^2	R^2 upper bound	R^2 lower bound
Arc15	1878	0.86	0.73	0.98	0.09	0.06	0.11
Ark1	260	0.32	0.21	0.42	0.12	0.05	0.20
Bzz1	2257	0.59	0.54	0.64	0.19	0.16	0.22
Ede1	252	0.29	0.14	0.45	0.05	0.01	0.12
Las17	582	0.97	0.82	1.12	0.21	0.16	0.28
Myo5	1202	1.13	1.00	1.26	0.19	0.15	0.23
Pan1	158	1.14	0.88	1.39	0.33	0.21	0.45
Rvs167	1802	0.37	0.31	0.43	0.08	0.06	0.11
Sac6	2512	0.91	0.81	1.02	0.10	0.08	0.13
Sla1	316	1.07	0.86	1.27	0.25	0.17	0.33
Sla2	274	0.73	0.59	0.88	0.28	0.19	0.37
Syp1	315	0.35	0.27	0.43	0.20	0.13	0.28
Vrp1	1604	0.96	0.88	1.04	0.24	0.21	0.28

Supplementary table 12: Fit statistics from linear fits of Abp1-RFP intensity vs. lifetime plots for GFP-tagged query proteins. Upper and lower bounds indicate the 95% confidence interval. Related to Figure 3D

Query protein	N	Slope	Slope upper bound	Slope lower bound	R^2	R^2 upper bound	R^2 lower bound
Arc15	1878	0.65	0.54	0.75	0.07	0.05	0.10
Ark1	260	0.19	0.04	0.34	0.02	0.00	0.07
Bzz1	2257	0.46	0.39	0.52	0.08	0.06	0.10
Ede1	252	-0.06	-0.24	0.12	0.00	0.03	0.01
Las17	582	0.96	0.76	1.16	0.13	0.08	0.18
Myo5	1202	0.95	0.79	1.11	0.10	0.07	0.14
Pan1	158	0.73	0.47	1.00	0.16	0.07	0.27
Rvs167	1802	0.28	0.22	0.35	0.04	0.02	0.06
Sac6	2512	0.70	0.60	0.80	0.07	0.05	0.09
Sla1	316	0.74	0.49	0.98	0.10	0.05	0.17
Sla2	274	0.50	0.31	0.70	0.09	0.03	0.16
Syp1	315	0.16	0.01	0.30	0.01	0.00	0.05
Vrp1	1604	0.59	0.49	0.70	0.07	0.05	0.09

Supplementary table 13: Fit statistics from linear fits of Ede1-RFP lifetime vs. lifetime plots for GFP-tagged query proteins. Upper and lower bounds indicate the 95% confidence interval. Related to Figure 4D

Query protein	N	Slope	Slope upper bound	Slope lower bound	R^2	R^2 upper bound	R^2 lower bound
Apl1	329	0.45	0.35	0.54	0.21	0.14	0.30
Hrr25	291	0.71	0.64	0.79	0.55	0.47	0.62
Pal1	207	0.64	0.53	0.75	0.39	0.29	0.49
Syp1	351	0.65	0.55	0.74	0.35	0.27	0.43

Supplementary table 14: Fit statistics from linear fits of Sla1-mCherry lifetime vs. lifetime plots for GFP-tagged query proteins. Upper and lower bounds indicate the 95% confidence interval. Related to Figure 4E

Query protein	N	Slope	Slope upper bound	Slope lower bound	R^2	R^2 upper bound	R^2 lower bound
Apl1	728	0.31	0.27	0.36	0.19	0.14	0.24
Ede1	260	0.17	0.09	0.25	0.06	0.02	0.13
Hrr25	444	0.09	0.04	0.14	0.03	0.00	0.06
Pal1	229	0.14	0.05	0.23	0.04	0.01	0.10
Syp1	211	0.20	0.13	0.28	0.12	0.05	0.21

Supplementary table 15: Fit statistics from linear fits of Abp1-RFP lifetime vs. lifetime plots for GFP-tagged query proteins. Upper and lower bounds indicate the 95% confidence interval. Related to Figure 4F

Query protein	N	Slope	Slope upper bound	Slope lower bound	R^2	R^2 upper bound	R^2 lower bound
Arc15	1878	0.66	0.63	0.69	0.59	0.56	0.61
Ark1	260	0.42	0.34	0.51	0.27	0.18	0.36
Bzz1	2257	0.23	0.20	0.26	0.11	0.09	0.14
Ede1	252	0.08	0.02	0.14	0.03	0.00	0.08
Las17	582	0.40	0.34	0.46	0.24	0.19	0.31
Myo5	1202	0.63	0.59	0.67	0.42	0.38	0.46
Pan1	158	0.24	0.13	0.35	0.10	0.03	0.21
Rvs167	1802	0.21	0.19	0.24	0.15	0.12	0.18
Sac6	2512	0.83	0.81	0.85	0.71	0.69	0.73
Sla1	316	0.24	0.16	0.33	0.09	0.04	0.16
Sla2	274	0.19	0.11	0.27	0.08	0.03	0.15
Syp1	315	-0.01	-0.07	0.05	0.00	0.02	0.01
Vrp1	1604	0.36	0.32	0.40	0.18	0.14	0.21

Supplemental References

Carroll SY, Stimpson HEM, Weinberg J, Toret CP, Sun Y, Drubin DG. 2012. Analysis of yeast endocytic site formation and maturation through a regulatory transition point. *Mol Biol Cell* **23**:657–668. doi:10.1091/mbc.E11-02-0108

Donovan KW, Bretscher a. 2015. Tracking individual secretory vesicles during exocytosis reveals an ordered and regulated process. *J Cell Biol* 1–14. doi:10.1083/jcb.201501118

Stimpson HEM, Toret CP, Cheng AT, Pauly BS, Drubin DG. 2009. Early-Arriving Syp1p and Ede1p Function in Endocytic Site Placement and Formation in Budding Yeast. *Mol Biol Cell* **20**:4640–4651. doi:10.1091/mbc.E09

Sun Y, Leong NT, Jiang T, Tangara A, Darzacq X, Drubin DG. 2017. Switch-like Arp2/3 activation upon WASP and WIP recruitment to an apparent threshold level by multivalent linker proteins in vivo. *Elife* **6**:1–25. doi:10.7554/elife.29140

Sun Y, Leong NT, Wong T, Drubin DG. 2015. A Pan1/End3/Sla1 complex links Arp2/3-mediated actin assembly to sites of clathrin-mediated endocytosis. *Mol Biol Cell* **26**:3841–3856. doi:10.1091/mbc.E15-04-0252